J. Fluid Mech. (2013), *vol.* 729, *pp.* 524–562.
doi:10.1017/jfm.2013.311

High-speed boundary-layer transition induced by a discrete roughness element

Prahladh S. Iyer and Krishnan Mahesh†

Department of Aerospace Engineering and Mechanics, University of Minnesota, Minneapolis, MN 55455, USA

(Received 19 June 2012; revised 28 February 2013; accepted 11 June 2013)

Direct numerical simulation (DNS) is used to study laminar to turbulent transition induced by a discrete hemispherical roughness element in a high-speed laminar boundary layer. The simulations are performed under conditions matching the experiments of Danehy *et al.* (*AIAA Paper* 2009–394, 2009) for free-stream Mach numbers of 3.37, 5.26 and 8.23. It is observed that the Mach 8.23 flow remains laminar downstream of the roughness, while the lower Mach numbers undergo transition. The Mach 3.37 flow undergoes transition closer to the bump when compared with Mach 5.26, in agreement with experimental observations. Transition is accompanied by an increase in C_f and C_h (Stanton number). Even for the case that did not undergo transition (Mach 8.23), streamwise vortices induced by the roughness cause a significant rise in C_f until $20D$ downstream. The mean van Driest transformed velocity and Reynolds stress for Mach 3.37 and 5.26 show good agreement with available data. Temporal spectra of pressure for Mach 3.37 show that frequencies in the range of 10–1000 kHz are dominant. The transition process involves the following key elements: upon interaction with the roughness element, the boundary layer separates to form a series of spanwise vortices upstream of the roughness and a separation shear layer. The system of spanwise vortices wrap around the roughness element in the form of horseshoe/necklace vortices to yield a system of counter-rotating streamwise vortices downstream of the element. These vortices are located beneath the separation shear layer and perturb it, which results in the formation of trains of hairpin-shaped vortices further downstream of the roughness for the cases that undergo transition. These hairpins spread in the span with increasing downstream distance and the flow increasingly resembles a fully developed turbulent boundary layer. A local Reynolds number based on the wall properties is seen to correlate with the onset of transition for the cases considered.

Key words: compressible boundary layers, transition to turbulence, high-speed flow

1. Introduction

The transition of boundary layers from laminar to turbulent flow has been an active field of research for several decades. Transition can occur due to several factors, e.g. free-stream disturbances, adverse pressure gradients and surface roughness. In this paper we study transition induced by isolated surface roughness in supersonic

† Email address for correspondence: mahesh@aem.umn.edu

and hypersonic boundary layers. For high-speed flows, transition is accompanied by an undesirable increase in the skin-friction coefficient and heating rates. Transition is therefore an important consideration for applications such as thermal protection systems for the Space Shuttle. Here, isolated roughness occurs in the form of steps, joints, rivets and local machining flaws.

Transition induced by an isolated roughness element at low speeds has been studied by Tani *et al.* (1962), Acarlar & Smith (1987) and Klebanoff, Cleveland & Tidstrom (1992) among others. Acarlar & Smith (1987) observe that a necklace-shaped vortex forms upstream of the hemispherical roughness and hairpin-shaped vortices are shed downstream of it. They suggest that the concentration of vorticity into the low-pressure recirculation region behind the roughness occurs in a manner so as to produce hairpin-shaped vortices. Tani *et al.* (1962) studied the effect of Re_k (Reynolds number based on the free-stream properties and roughness height) and showed that increasing Re_k beyond a critical value moves the transition location closer to the roughness. They suggest that the deformation of the velocity field due to the streamwise vortices (observed even at subcritical Re_k) shed on the sides of the hemisphere is likely to account for the critical behaviour of transition. Tumin & Reshotko (2005) studied the receptivity of a boundary layer past a three-dimensional hump and found that counter-rotating streamwise vortices were produced downstream of the roughness. Ergin & White (2006) experimentally studied the flow past an array of cylinders placed on a flat plate. They note that the transition process is a result of a competition between the unsteady disturbance growth and the rapid relaxation of the steady flow that tends to stabilize disturbances. Mason & Morton (1987) experimentally studied the flow behind wall-mounted obstacles and found that counter-rotating streamwise vortices were formed at the centre plane. Depending on the shape of the obstacle, the vortices had an upwash or downwash.

While incompressible transition is sensitive to Reynolds number and the shape and height of the roughness element, transition at high speeds also depends on the Mach number, free-stream temperature and the thermal boundary condition at the wall. Also, the influence of shock waves produced by the roughness on transition location is unclear. Schneider (2008) provides a review of the effects of roughness on the transition of hypersonic boundary layers. Some of the suggested mechanisms for hypersonic boundary layer transition include the concave-wall Görtler instability (Saric 1994), the first- and second-mode streamwise instability (Mack 1984), the three-dimensional cross-flow instability (Saric, Reed & White 2003) and transient growth (Reshotko & Tumin 2004). Empirical correlations based on Re_θ/M_e (Reshotko 2007) and Re_{kk} (Reda 2002) (Reynolds number based on properties at the height of the roughness) are used to predict the onset of transition, with varying amounts of success. Linear stability theory (LST) has been widely used to study transition in compressible flows, e.g. Lees & Lin (1946), Mack (1984) and Malik (1990). Typically for boundary layers, a locally parallel assumption is made wherein the mean flow varies in the wall-normal direction only and the e^N method, which is a measure of the integrated growth rates of the linear instability waves, is used to predict the onset of transition. While two-dimensional Tollmein–Schlichting (TS) waves are the most unstable mode at low speeds, oblique and inviscid Mack modes tend to be the most unstable modes at high-speeds depending on M_∞ and wall conditions. Under many circumstances, the linear eigenmode growth is 'bypassed'. Reshotko (2001) lists the various paths to transition to turbulence depending on the amplitude of the disturbance. For low-amplitude disturbances, linear eigenmode growth takes place, followed by secondary instability, mode interactions and nonlinear breakdown. Even when the

flow is asymptotically stable to small disturbances, algebraic growth could take place, termed as transient growth (Reshotko & Tumin 2004). For large disturbance levels, nonlinear breakdown takes place which cannot be described by the linearized disturbance equations.

The availability of greater computational resources and parallel computing have enabled the use of direct numerical simulations (DNS) to study transition. A recent review by Zhong & Wang (2012) discusses the progress made in the DNS of instability and transition in hypersonic boundary layers. Chang & Choudhari (2009) numerically studied transition induced by large roughness elements using the space–time conservation element solution element (CESE) methodology. They simulated flow around rectangular and cylindrical elements in boundary layers at Mach numbers of 4.1 and 6.5 and concluded that for these Mach numbers, no self-sustaining vortex-generation process was present. They also performed a two-dimensional parametric study and found that at subcritical Reynolds numbers of the boundary layer, absolute instability resulting in vortex shedding downstream was likely to weaken at supersonic free-stream conditions. They therefore conjectured that convective instability might be the dominant instability mechanism for supersonic boundary layers. They also noted the presence of 'mushroom-shaped' streamwise velocity contours in the wake which give rise to inflexion points in the flow downstream. Redford, Sandham & Roberts (2010) studied the flow past a smooth shaped roughness element at Mach 3 and 6 with acoustic forcing at the free stream to ensure transition. They proposed a correlation for predicting transition induced by a three-dimensional roughness element at high speeds for roughness heights smaller than the boundary-layer thickness. Bartkowicz, Subbareddy & Candler (2010) studied the effect of a cylindrical protuberance on a Mach 6 laminar boundary layer using DNS. They observed that the vortex system formed upstream of the cylinder resembles the set of vortices seen in incompressible flow by Baker (1979) and concluded that for thinner boundary layers, the shock created by the roughness produces a jet of high momentum fluid that recirculates into the vortex system which could cause unsteadiness.

Marxen, Iaccarino & Shaqfeh (2010) studied Mach 4.8 flow past a two-dimensional roughness using a body fitted grid and immersed boundary technique. They found that the roughness considerably alters the stability characteristics of the flow, although far downstream the stability characteristics resemble that of a flat plate boundary layer. Groskopf, Kloker & Marxen (2008) performed a biglobal stability analysis of the region downstream of a three-dimensional pizza-box-shaped roughness and noted a pronounced convective instability due to a pair of counter-rotating streamwise vortices. Choudhari *et al.* (2010) studied the biglobal stability characteristics behind a diamond shaped roughness and a pair of roughness elements at Mach 3.5. They study the even (symmetric/varicose) and odd (antisymmetric/sinuous) modes of instability produced by the roughness. They note that the fluctuations associated with either modes are concentrated over a narrow spanwise extent of the streaks, which is significantly smaller in comparison with the spanwise wavelength of the dominant first mode instability of the dominant first mode instability of the unperturbed boundary layer flow.

The present study is a case of bypass transition where the roughness is taller than the laminar boundary-layer thickness at its location if it were absent. Hence, the resulting perturbations are no longer small; they change the base flow itself instead of being linear perturbations of the boundary layer. This suggests the use of DNS of the compressible Navier–Stokes equations as a means to study the physical mechanism

of transition. This paper uses DNS to analyse the flow features produced due to the roughness element at supersonic and hypersonic speeds and assess their role in transition. Flow past an isolated hemispherical bump at Mach 3.37, 5.26 and 8.23 are studied at conditions that match the experiments by Danehy *et al.* (2009). We use a novel algorithm developed by Park & Mahesh (2007) to simulate compressible flows on unstructured grids. It employs a modified least-squares approach to reconstruct the fluxes at cell faces (that makes the convective flux computation more accurate) and a scheme to split the viscous stress tensor into the compressible and the incompressible parts (that makes the viscous flux computation accurate). A characteristic filter based shock capturing scheme provides stable solutions in the presence of discontinuities.

The algorithm is described in § 2, and validated against temporal LST for a two-dimensional $M_\infty = 2.0$ Couette flow and a $M_\infty = 4.5$ boundary layer in § 3. Section 4 describes the set-up of the simulation, flow parameters and results from a grid convergence study. Section 5 qualitatively compares the flow field observed in our simulation with those observed from the experiment. Section 6 describes the various flow features associated along with a description of the proposed transition mechanism. Temporal spectra and a comparison of mean statistics for Mach 3.37 with a turbulent boundary layer are reported in § 6. A brief summary in § 7 concludes the paper.

2. Algorithm details

The simulations use an algorithm developed by Park & Mahesh (2007) for solving the compressible Navier–Stokes equations on unstructured grids:

$$\frac{\partial \rho}{\partial t} = -\frac{\partial}{\partial x_k}\left(\rho u_k\right) \tag{2.1}$$

$$\frac{\partial \rho u_i}{\partial t} = -\frac{\partial}{\partial x_k}\left(\rho u_i u_k + p\delta_{ik} - \sigma_{ik}\right) \tag{2.2}$$

$$\frac{\partial E_T}{\partial t} = -\frac{\partial}{\partial x_k}\left\{\left(E_T + p\right) u_k - \sigma_{ik} u_i - Q_k\right\} \tag{2.3}$$

where ρ, u_i, p and E_T are the density, velocity, pressure and total energy, respectively. The viscous stress σ_{ij} and heat flux Q_i are given by

$$\sigma_{ij} = \frac{\mu}{Re}\left(\frac{\partial u_i}{\partial x_j} + \frac{\partial u_j}{\partial x_i} - \frac{2}{3}\frac{\partial u_k}{\partial x_k}\delta_{ij}\right) \tag{2.4}$$

$$Q_i = \frac{\mu}{(\gamma - 1)M_\infty^2 RePr}\frac{\partial T}{\partial x_i} \tag{2.5}$$

where Re, M_∞ and Pr denote the Reynolds number, Mach number and Prandtl number, respectively.

The governing equations are discretized using a cell-centred finite-volume scheme, a schematic of which is shown in figure 1(*a*). Upon integration over the control volume (CV), application of the Gauss theorem and some rearrangement, the governing equations may be written as

$$\frac{\partial \rho_{cv}}{\partial t} = -\frac{1}{V_{cv}}\sum_{faces} \rho_f v_N A_f \tag{2.6}$$

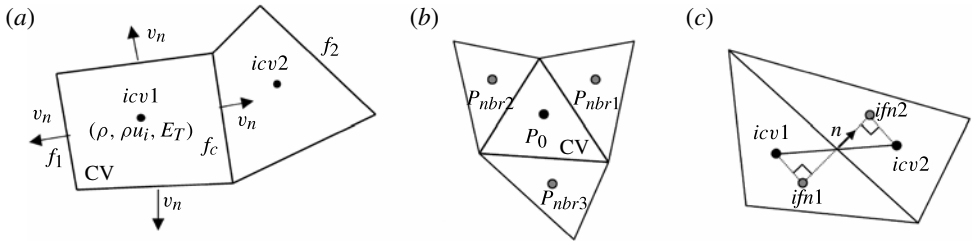

FIGURE 1. Schematic of the finite-volume scheme used with (*a*) depicting the collocated cell-centred scheme used, (*b*) depicting the cell centre P_0 and its neighbouring points used for least-squares reconstruction and (*c*) depicting the projection of the control volume (CV) centre onto the face normal for computing derivatives at the face for viscous terms.

$$\frac{\partial(\rho u_i)_{cv}}{\partial t} = -\frac{1}{V_{cv}} \sum_{faces} \left[(\rho u_i)_f v_N + p_f n_i - \sigma_{ik,f} n_k\right] A_f \tag{2.7}$$

$$\frac{\partial(E_T)_{cv}}{\partial t} = -\frac{1}{V_{cv}} \sum_{faces} \left[(E_T + p)_f v_N - \sigma_{ik,f} u_{i,f} n_k - Q_{k,f} n_k\right] A_f \tag{2.8}$$

where V_{cv} is the volume of CV, A_f is the area of the face, n_i is the outward normal vector at surface and v_N is the face-normal velocity.

Here $\boldsymbol{q}_{cv} = (\int_{cv} \boldsymbol{q}\, \mathrm{d}V)/V_{cv}$ is the volume average within the cell, where $\boldsymbol{q} = (\rho, \rho u_i, E_T)$ are the conservative variables. Here, the subscript f denotes interpolation at each face of the control volume. For any scalar ϕ, the value at the face is computed as follows,

$$\phi_{f_c} = \frac{\phi_{icv1} + \phi_{icv2}}{2} + \frac{1}{2}(\nabla\phi|_{icv1} \cdot \Delta\boldsymbol{x}^{icv1} + \nabla\phi|_{icv2} \cdot \Delta\boldsymbol{x}^{icv2}), \tag{2.9}$$

where $\Delta\boldsymbol{x}^{icv1} = \boldsymbol{x}_{f_c} - \boldsymbol{x}_{icv1}$ and $\nabla\phi|_{icv1}$ denotes the gradient defined at $icv1$. The gradient is computed using the 'least-squares method' (LSQ) for viscous terms and the 'modified least-squares method' (MLSQ) for the convective terms.

In the LSQ method, $\nabla\phi|_{cv}$ is computed using the Taylor series expansion given by

$$\phi(\boldsymbol{x}) \approx \phi(\boldsymbol{x}_0) + \nabla\phi|_{cv} \cdot (\boldsymbol{x} - \boldsymbol{x}_0), \tag{2.10}$$

where $\boldsymbol{x}_0$ denotes coordinates of the CV cell centre, P_0 in figure 1(*b*), and $\boldsymbol{x}$ is any point that belongs to neighbouring cells. Let $\nabla\phi|_{cv} = (\mathscr{A}, \mathscr{B}, C)$, then the best choice of $\nabla\phi|_{cv}$ is that which minimizes the functional

$$F(\mathscr{A}, \mathscr{B}, C) = \sum_{nbr} \left[\phi_{nbr} - \phi(\boldsymbol{x}_0) - (\mathscr{A}, \mathscr{B}, C) \cdot (\boldsymbol{x}_{nbr} - \boldsymbol{x}_0)\right]^2 w_{nbr}, \tag{2.11}$$

where ϕ_{nbr} and $\boldsymbol{x}_{nbr}$ denote the values and locations of neighbour cells shown in figure 1(*b*). Here w_{nbr} is the weighting function, which is set to be 1 for simplicity

and to preserve the symmetry of the scheme. From the condition $\partial F/\partial \mathscr{A} = \partial F/\partial \mathscr{B} = \partial F/\partial \mathscr{C} = 0$, $\nabla\phi|_{cv}$ is given by the solution of the system

$$\begin{bmatrix} \sum_{nbr} \Delta x^2 & \sum_{nbr} \Delta x\Delta y & \sum_{nbr} \Delta x\Delta z \\ \sum_{nbr} \Delta x\Delta z & \sum_{nbr} \Delta y^2 & \sum_{nbr} \Delta y\Delta z \\ \sum_{nbr} \Delta x\Delta z & \sum_{nbr} \Delta y\Delta z & \sum_{nbr} \Delta z^2 \end{bmatrix} \begin{pmatrix} \mathscr{A} \\ \mathscr{B} \\ \mathscr{C} \end{pmatrix} = \begin{pmatrix} \sum_{nbr} \Delta\phi_{nbr}\Delta x \\ \sum_{nbr} \Delta\phi_{nbr}\Delta y \\ \sum_{nbr} \Delta\phi_{nbr}\Delta z \end{pmatrix}, \tag{2.12}$$

where $\Delta x = x_{nbr} - x_0$, $\Delta\phi_{nbr} = \phi_{nbr} - \phi_0$ and other terms are defined similarly.

In the MLSQ method, the Gauss divergence theorem is invoked to compute $\nabla\phi|_{cv}$ as follows:

$$\nabla\phi|_{cv} = \frac{1}{V_{cv}} \sum_{faces} \phi^{\star}_{f_c} n_i A_f. \tag{2.13}$$

Here $\phi^{\star}_{f_c}$ is evaluated as a simple average of the values at the cell centres sharing the face:

$$\phi^{\star}_{f_c} = 0.5(\phi_{icv1} + \phi_{icv2}). \tag{2.14}$$

Note that both the LSQ and MLSQ methods of obtaining the quantities at the face using (2.9) are second-order accurate. Also, for uniform structured grids, the LSQ and MLSQ methods reduce to the same formula for evaluating quantities at the face. For a uniform one-dimensional grid with spacing Δx, (2.9) using either LSQ or MLSQ reduces to a second-order interpolation formula given by

$$\phi_{i+(1/2)} = \tfrac{1}{8}\left(-\phi_{i+2} + 5\phi_{i+1} + 5\phi_i - \phi_{i-1}\right), \tag{2.15}$$

where $\phi_{i+(1/2)}$ is the value at cell face and ϕ_i, $\phi_{i+1}, \ldots$ are cell centre values. The corresponding finite difference is

$$\left.\frac{\delta\phi}{\delta x}\right|_i = \frac{-\phi_{i+2} + 6\phi_{i+1} - 6\phi_{i-1} + \phi_{i-2}}{8\Delta x}. \tag{2.16}$$

Park & Mahesh (2007) show that the current method of face reconstruction (obtaining derivatives) has better modified wavenumber properties when compared with a non-compact fourth-order central difference stencil.

The viscous terms involves the computation of σ_{ij} which is given by

$$\sigma_{ij,f} = \left(\frac{\mu}{Re}\right)_f \left(\left.\frac{\partial u_i}{\partial x_j}\right|_f + \left.\frac{\partial u_j}{\partial x_i}\right|_f - \frac{2}{3}\left.\frac{\partial u_k}{\partial x_k}\right|_f \delta_{ij} \right). \tag{2.17}$$

To compute the viscous stresses, we split the term into two parts. $\sigma_{ij} = \sigma^1_{ij} + \sigma^2_{ij}$ where $\sigma^1_{ij} = (\mu/Re)(\partial u_i/\partial x_j)$ and $\sigma^2_{ij} = (\mu/Re)((\partial u_j/\partial x_i) - (2/3)(\partial u_k/\partial x_k)\delta_{ij})$. Here σ^2_{ij} can be interpreted as the compressible part, since it vanishes in the incompressible limit. Then, σ^1_{ij} is computed by

$$\frac{1}{V_{cv}} \sum_{faces} \left(\frac{\mu}{Re}\right)_f \left.\frac{\partial u_i}{\partial x_j}\right|_f n_j A_f = \frac{1}{V_{cv}} \sum_{faces} \left(\frac{\mu}{Re}\right)_f \left.\frac{\partial u_i}{\partial n}\right|_f A_f. \tag{2.18}$$

Here, the normal gradient at the face is computed by

$$\frac{\partial \phi}{\partial n} = \frac{\phi_{ifn2} - \phi_{ifn1}}{d_f}, \tag{2.19}$$

where $ifn1$ ($ifn2$) is the projection of $icv1$ ($icv2$) onto the extension of normal vector $\boldsymbol{n}$ as illustrated in figure 1(c), and d_f is the distance between $ifn1$ and $ifn2$. Here ϕ_{ifn1} is given by

$$\phi_{ifn1} = \phi_{icv1} + \nabla\phi|_{icv1} \cdot (\boldsymbol{x}_{ifn1} - \boldsymbol{x}_{icv1}), \tag{2.20}$$

where a LSQ method is used to obtain $\nabla\phi$ at $icv1$.

Viscosity at the cell face is given by (2.9) and LSQ reconstruction. Here $\sigma^2_{ij,f}$ is constructed by the interpolation of $\sigma^2_{ij}|_{icv1}$ and $\sigma^2_{ij}|_{icv2}$ using (2.9). Again, the LSQ method is used for all spatial derivatives at cell centres.

The solution is advanced in time using a second-order explicit Adams–Bashforth scheme in a predictor–corrector fashion wherein a shock-capturing scheme is applied in the corrector step as illustrated below:

$$\hat{\boldsymbol{q}}^{n+1}_{cv} = \boldsymbol{q}^{n}_{cv} + \frac{\Delta t}{2}\left[3rhs_{cv}(\boldsymbol{q}^{n}) - rhs_{cv}(\boldsymbol{q}^{n-1})\right], \tag{2.21}$$

$$\boldsymbol{q}^{n+1}_{cv} = \hat{\boldsymbol{q}}^{n+1}_{cv} - \frac{\Delta t}{V_{cv}} \sum_{faces} \left(\boldsymbol{F}^{*}_{f} \cdot \boldsymbol{n}_f\right) A_f, \tag{2.22}$$

where rhs_{cv} represents the right-hand side of (2.6)–(2.8) and $\boldsymbol{F}^{*}_{f}$ is the filtered numerical flux. The algorithm uses a novel filter-based shock-capturing scheme that localizes numerical dissipation to the vicinity of flow discontinuities. Once the solution is advanced from $\boldsymbol{q}^{n}_{cv}$ to $\hat{\boldsymbol{q}}^{n+1}_{cv}$, the final solution $\boldsymbol{q}^{n+1}_{cv}$ is determined from a corrector scheme (equation (2.22)) similar to the approach of Yee, Sandham & Djomehri (1999). The characteristic-based filter proposed by Yee *et al.* (1999) to compute $\boldsymbol{F}^{*}_{f}$ is extended to unstructured grids by Park & Mahesh (2007). The filter numerical flux has the form

$$\boldsymbol{F}^{*}_{fc} = \tfrac{1}{2}\boldsymbol{R}_{fc}\,\boldsymbol{\Phi}^{*}_{fc}, \tag{2.23}$$

where $\boldsymbol{R}$ is the right Eigenvector of $[\rho_f v_N, (\rho u_i)_f v_N + p_f n_i, (E_T + p)_f v_N]^{\mathrm{T}}$ $(i = 1, 2, 3)$. The face value $\boldsymbol{R}_{fc} = \boldsymbol{R}(\boldsymbol{q}_{icv1}, \boldsymbol{q}_{icv2})$ is constructed using Roe's average:

$$\boldsymbol{u}_{fc,Roe} = \frac{\sqrt{\rho_{icv1}}\boldsymbol{u}_{icv1} + \sqrt{\rho_{icv2}}\boldsymbol{u}_{icv2}}{\sqrt{\rho_{icv1}} + \sqrt{\rho_{icv2}}}, \tag{2.24a}$$

$$H_{fc,Roe} = \frac{\sqrt{\rho_{icv1}}H_{icv1} + \sqrt{\rho_{icv2}}H_{icv2}}{\sqrt{\rho_{icv1}} + \sqrt{\rho_{icv2}}}, \tag{2.24b}$$

$$c^2_{fc,Roe} = (\gamma - 1)\left[H_{roe} - \frac{1}{2}\left(u^2_{fc,Roe} + v^2_{fc,\mathrm{Roe}} + w^2_{fc,Roe}\right)\right], \tag{2.24c}$$

where $H = (E_t + p)/\rho$ is the enthalpy and c is the speed of sound. On the other hand, the expression for the ℓth component of $\boldsymbol{\Phi}^{*}$, $\phi^{*\ell}$ is given by

$$\phi^{*\ell}_{fc} = \kappa\theta^{\ell}_{fc}\phi^{\ell}_{fc}, \tag{2.25}$$

where κ is the adjustable parameter and θ_{fc} is the switch function given by

$$\theta_{fc} = \sqrt{0.5\left(\hat{\theta}^2_{icv1} + \hat{\theta}^2_{icv2}\right)}, \tag{2.26a}$$

$$\hat{\theta}_{icv1} = \left| \frac{|\alpha_{fc}| - |\alpha_{f_1}|}{|\alpha_{fc}| + |\alpha_{f_1}|} \right|^p, \tag{2.26b}$$

$$\hat{\theta}_{icv2} = \left| \frac{|\alpha_{f_2}| - |\alpha_{fc}|}{|\alpha_{f_2}| + |\alpha_{fc}|} \right|^p. \tag{2.26c}$$

Here, $\alpha_f = \boldsymbol{R}_f^{-1} \Delta \boldsymbol{q} = \boldsymbol{R}_f^{-1} (\boldsymbol{q}_{icv2} - \boldsymbol{q}_{icv1})$ is the difference of the characteristic variable across the face, and $p = 1$ is used. The reader is referred to Park & Mahesh (2007) for further details of the algorithm. Note that no explicit filtering is performed in the code.

The numerical method been used to study transition to turbulence induced by distributed roughness in a Mach 2.9 boundary layer in Muppidi & Mahesh (2012) and transition to turbulence using blowing and suction at Mach 2.25 in Muppidi & Mahesh (2010) where the turbulent statistics showed good agreement with experimental data under similar conditions. The algorithm has also been used to study the interaction of a supersonic jet with a subsonic cross-flow and a sonic jet with a supersonic cross-flow in Chai & Mahesh (2011), where a comparison of mean velocity profiles showed good agreement with experiments. Also, DNS of shock–turbulence interaction at Mach 2.9 in a compression corner was studied in Muppidi & Mahesh (2011) using the current methodology.

3. Validation with LST

The algorithm described in § 2 is validated against LST to demonstrate its suitability for transitional simulations. We follow closely the analysis by Zhong (1998) and Dong & Zhong (2002) and present results for a supersonic Couette flow at $M_\infty = 2.0$ and a supersonic boundary layer at $M_\infty = 4.5$. The linear stability code uses a second-order staggered finite difference scheme (2FD) proposed by Malik (1990) for a locally parallel flow (wherein the base flow varies in y only) and has been validated against all of the cases presented in Malik (1990). The non-conservative form of the Navier–Stokes equations is linearized about the base flow obtained from a similarity solution. Defining $\phi = \{u, v, p, T, w\}^{\mathrm{T}}$ and expanding in the normal mode form,

$$\tilde{\phi} = \hat{\phi} \mathrm{e}^{\mathrm{i}(\alpha x + \beta z - \omega t)} \tag{3.1}$$

where $\tilde{\phi}$ represents the perturbation of the quantity, α and β are the streamwise and spanwise wavenumbers and ω is the angular frequency, we obtain an eigenvalue problem for ω (temporal theory) or α (spatial theory). We use the temporal theory for two-dimensional disturbances where α is real, $\beta = 0$ and ω is complex for our comparison. The DNS is initialized with the eigenmode obtained from the linear stability code and the nonlinear Navier–Stokes equations are solved using the finite-volume algorithm described in § 2. Here $\boldsymbol{q} = (\rho, \rho u_i, E_T)$ is initialized as follows: $\boldsymbol{q} = \bar{\boldsymbol{q}}(\boldsymbol{y}) + \epsilon Re(\tilde{\boldsymbol{q}})$ where $\bar{q}(y)$ is obtained from the similarity solution, $\tilde{q}$ is obtained from $\tilde{\phi}$ obtained from the LST code and $\epsilon = 0.001$ for both of the validation cases presented.

For the Couette flow problem, $M_\infty = 2$ and $Re_\infty = 1000$ (based on spacing between the walls). The upper wall is an isothermal wall with $T_\infty = 220.667$ K while the lower wall is an adiabatic wall. The fluid is assumed to be an ideal gas with $\gamma = 1.4$ and $Pr = 0.72$. Sutherland's law is used to compute viscosity. The DNS is initialized with a stable mode which has a dimensionless wavenumber $\alpha = 3.0$. The eigenvalue obtained from temporal LST is $\omega = 5.524\,567 - \mathrm{i}0.134\,598$ for stretched grid using 100 points. Figure 2 shows results from DNS compared with LST for validation. The

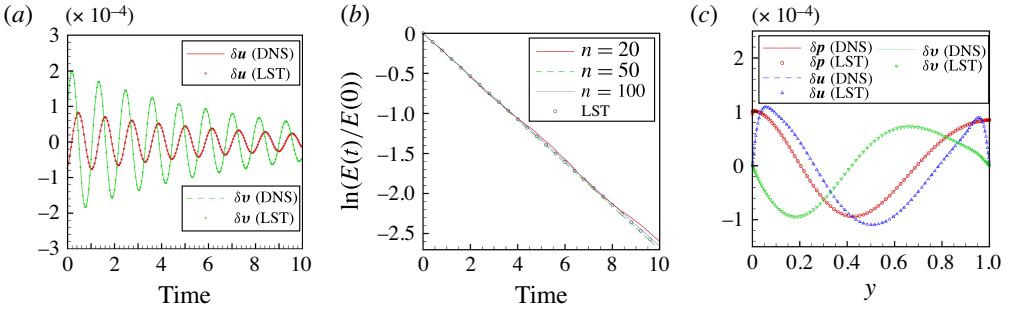

FIGURE 2. (Colour online) Validation with LST for Couette flow with (*a*) showing the time variation of perturbation velocities at a point in the domain, (*b*) showing the variation of perturbation kinetic energy of the domain with time where N indicates the number of points in y and (*c*) showing the wall-normal variation of perturbation quantities at $x = 0.963$.

DNS is carried out in a two-dimensional domain covering one wavelength of $\alpha = 3.0$ in the x-direction. Periodic boundary conditions are used in the streamwise direction. The DNS was carried out using a 50×20, 50×50 and 100×100 grids with uniform grid spacing in the streamwise direction.

Figure 2(*a*) shows the comparison of disturbance velocities obtained from DNS and LST for a 100×100 grid at a random location in the domain and we see that the agreement is good. To compare the amplification rate (ω_i) from DNS to LST, we plot the perturbation kinetic energy with time in figure 2(*b*). From LST, the perturbation kinetic energy is given by

$$E(t) = \int\int \frac{1}{2}(u'^2 + v'^2)\,\mathrm{d}x\,\mathrm{d}y = E_0 \mathrm{e}^{2\omega_i t}, \tag{3.2}$$

where E_0 is the initial perturbation energy. We see that the good agreement is observed between the expected ω_i and that obtained from DNS. Figure 2(*c*) shows the variation of perturbation quantities with y at $x = 0.963$ from DNS and LST after 5 units of time for a 100×100 grid and we see that the agreement is good.

For the boundary-layer flow problem, $M_\infty = 4.5$ and $Re_\infty = 1500$ (based on the boundary-layer scaling $l = \sqrt{\nu_\infty x/u_\infty}$). Here y_{max} is set to 100, $T_\infty = 121$ K and the wall is set to be adiabatic. The flow conditions are the same as in a test case of Malik (1990) with the same grid stretching being used here. The DNS is initialized with an unstable mode which has a dimensionless wavenumber $\alpha = 0.25$. The grid in the y direction is identical in the DNS and LST computations. The eigenvalue obtained from temporal LST is $\omega = 0.227\,491 + \mathrm{i}0.002\,296$ for stretched grid using 300 points. Figure 3 shows results from DNS compared with LST for validation. The DNS is carried out in a two-dimensional domain covering one wavelength of $\alpha = 0.25$ in the x direction. Periodic boundary conditions are used in the streamwise direction. The DNS was carried out using a 100×50, 100×100, 100×200 and 100×300 grids with uniform grid spacing in the streamwise direction. The 100×100 grid has approximately 60 points within the boundary layer and is representative of the fine grid used in the roughness-induced transition study.

Figure 3(*a*) shows the comparison of disturbance velocities obtained from DNS and LST for a 100×100 grid at a random location in the domain and we see that the agreement is good. To compare the amplification rate (ω_i) from DNS to LST, we plot

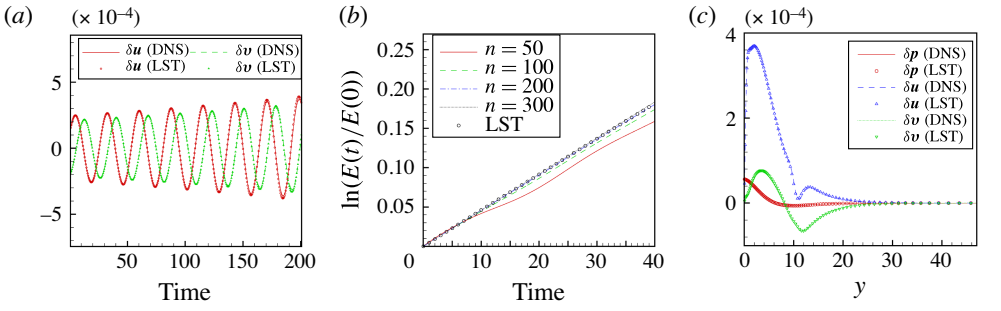

FIGURE 3. (Colour online) Validation with LST for boundary layer flow with (*a*) showing the time variation of perturbation velocities at a point in the domain, (*b*) showing the variation of perturbation kinetic energy of the domain with time where N indicates the number of points in y and (*c*) showing the wall-normal variation of perturbation quantities at the inflow plane.

the perturbation kinetic energy with time in figure 3(*b*). We see that good agreement is observed between the expected ω_i and that obtained from DNS. Figure 3(*c*) shows the variation of perturbation quantities with y at the inflow plane after 100 units of time for a 100×100 grid from DNS and LST and we see that the agreement is good.

4. Problem description

4.1. *Simulation parameters*

Flow past a hemispherical bump placed on a flat plate is simulated at conditions that match the experiments of Danehy *et al.* (2009). The experimental set-up consists of a wedge placed at different angles to an incoming Mach 10 flow at 51.32 K with unit Reynolds number $Re = 6$ million m^{-1}. A hemispherical roughness element of 4 mm diameter (denoted by D) is placed on the top surface of the wedge at a distance of 75.4 mm ($18.85D$) from the leading edge of the wedge. The top surface of the wedge is 157.2 mm ($39.3D$) long and 127 mm ($31.75D$) wide. A shock wave forms at the leading edge of the wedge and post-shock conditions yield the free-stream conditions for the top surface of the wedge (and the roughness element). The wedge was placed at different angles to the Mach 10 flow to yield different free-stream conditions. Three such conditions are simulated and are listed in table 1. In addition to free-stream density, velocity and temperature, table 1 also lists the free-stream Mach number, k/δ and roughness Reynolds number ($Re_k = u_\infty k/\nu_\infty$) computed based on free-stream properties and the height of the roughness ($k = D/2 = 2$ mm). Here δ is the boundary layer thickness at the location of the roughness if it were absent. The wall is maintained at a constant temperature of 300 K, and T_w/T_{aw} is roughly constant for all cases at 0.3 since the wall temperature and the stagnation temperature of the wind tunnel facility is maintained constant for all cases. Here T_{aw} is the adiabatic wall temperature computed using the following relation: $T_{aw} = T_\infty(1 + 0.5r(\gamma - 1)M_\infty^2)$ where r is the recovery factor taken to be 0.85.

The simulations model the post-shock flow over the top surface of the wedge as flow over a flat plate. The flow conditions upstream of the wedge were obtained from Danehy *et al.* (2009), and post-shock conditions obtained from the Rankine–Hugoniot equations were specified as free-stream conditions for the flat plate. The compressible

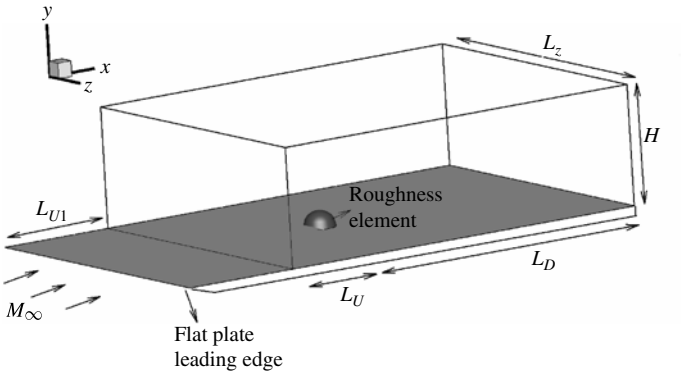

FIGURE 4. Schematic of the problem used in this study. The box depicts the computational domain where a compressible similarity solution is prescribed at the inflow.

M_∞	u_∞ (m s^{-1})	ρ_∞ (kg m^{-3})	T_∞ (K)	k/δ	Re_k	Re_θ
3.37	1217.57	0.0786	340.48	2.54	9121	375.59
5.26	1344.85	0.0647	162.90	2.08	14 190	447.80
8.23	1409.86	0.0328	73.12	1.19	16 831	493.42

TABLE 1. Simulation parameters. Here $T_{wall} = 300$ K for all cases, $Re_k = u_\infty k/\nu_\infty$ and $Re_\theta = u_\infty \theta/\nu_\infty$.

Navier–Stokes equations are solved in non-dimensional form as follows:

$$\rho = \rho^*/\rho^*_\infty \quad u = u^*/u^*_\infty \quad T = T^*/T^*_\infty \quad p = p^*/\rho^*_\infty u^{*2}_\infty \quad x_i = x^*_i/D \quad t = t^* u_\infty/D, \quad (4.1)$$

where the asterisk ($*$) denotes dimensional values. A schematic of the computational domain is shown in figure 4. The inflow of the computational domain is at a distance of $8.85D$ from the leading edge of the flat plate. A compressible boundary-layer similarity solution is prescribed at the inflow domain to yield the experimental boundary-layer thickness at the location of the roughness if it were absent. Distances L_U, L_D, L_z and H are defined as shown in figure 4. Three grids were used for this study which are described in § 4.2. Here $L_U = 10D$ for all of the cases and $L_D = 40D$. The height of the domain (H) is $10D$ for the coarser grids and $6D$ for the fine grid while $L_z = 40D$ for the coarser grids and $20D$ for the fine grid.

Figure 5 illustrates the instantaneous flow features for the Mach 3.37 flow. Density gradient contours are shown in the symmetry and streamwise planes to depict the shock while streamwise vorticity (ω_x) is shown in the plane parallel to the flat plate. Far upstream the flow is laminar while unsteady flow features can be observed downstream of the roughness. The unsteady region spreads in the span with increasing downstream distance from the roughness. Note the system of shocks produced due to the roughness. The separation shock is produced when the supersonic inflow comes into contact with the separated low-speed fluid. The roughness element produces a shock which is the strongest of the system of shocks formed followed by the reattachment shock formed due to the compression of the fluid reattaching the flat plate downstream of the roughness. The three-dimensional nature of the shock is

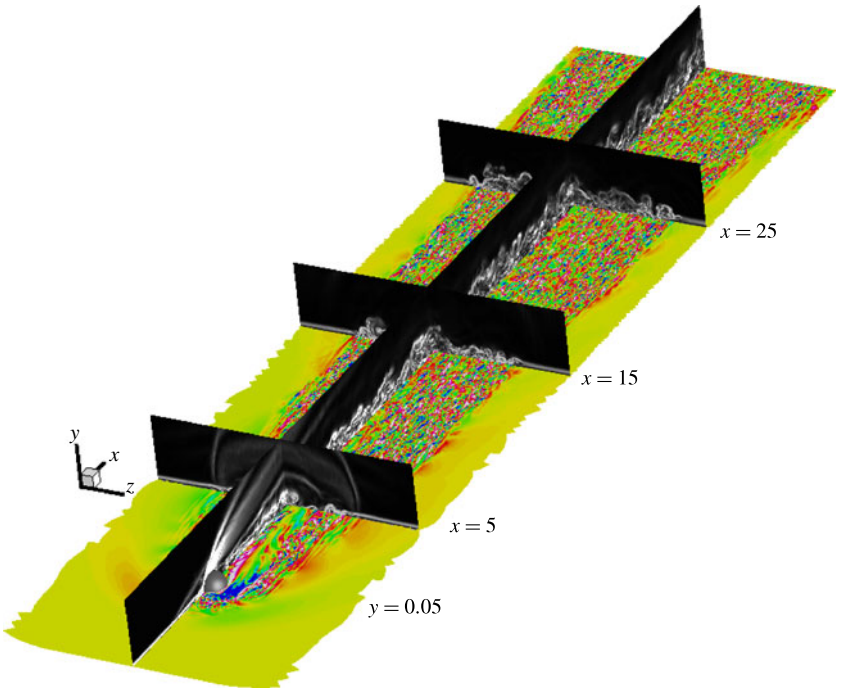

FIGURE 5. (Colour online) An instantaneous snapshot of the flow for Mach 3.37. Density gradient contours are shown in the symmetry and streamwise planes to show the shocks and vortices. Streamwise vorticity contours are shown in the $y = 0.05$ plane showing small scale features of the flow far downstream.

visible in the streamwise plane closest to the roughness. Far downstream, the small-scale vortical structures are indicative of a turbulent flow.

4.2. *Grid parameters*

Three different grids were used in this study which are referred to as 'coarse', 'medium' and 'fine' in this section. The coarse and medium grids were refined in the vicinity of the bump with increasing Δx spacing towards the outflow. In the finest grid, Δx spacing was maintained constant throughout the region downstream of the roughness to capture the turbulent region. Since the Mach 8.23 boundary layer did not undergo transition, a relatively coarse grid of 16 million was used. For the Mach 3.37 and 5.26 simulations, the mesh spacings were chosen based on the coarse grid results so as to maintain $\Delta x^+ = 15$, $\Delta y^+_{min} = 0.6$ ($\Delta y^+_{cv} = 0.3$) and $\Delta z^+ = 10$ for the finest grid in the region downstream of the roughness. The viscous spacings of $\Delta x^+ = 15$ and $\Delta z^+ = 10$ corresponds to $\Delta x = 0.02$ and $\Delta z = 0.0133$ for $M_\infty = 3.37$, and $\Delta x = 0.04$ and $\Delta z = 0.0266$ for $M_\infty = 5.26$, respectively. The grid is finer in the vicinity of the roughness with more than 240 points on the surface of the roughness in the $y = 0$ plane for all three grids used.

The symmetry and wall-parallel planes of the grid in the vicinity of the roughness are shown in figure 6. Note that the region near the roughness element is much finer than the surrounding regions. Since the transitional/turbulent region generated due to the roughness is confined within a certain span, Δz quickly coarsens outside the wake of the roughness (figure 7). The finest grid for Mach 3.37 contained approximately 154

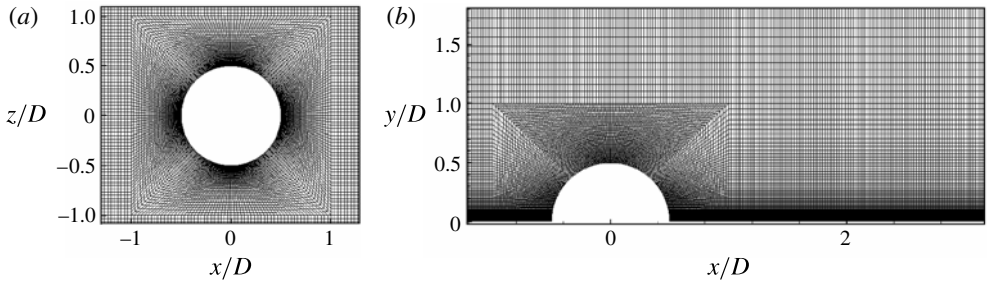

FIGURE 6. Wall-parallel (*a*) and symmetry planes (*b*) showing the grid used in hemispherical bump simulation for Mach 3.37. Note that the grid is highly refined in the vicinity of the roughness and derefined away from it.

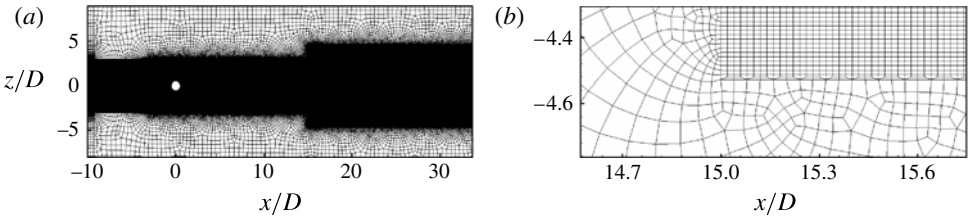

FIGURE 7. Wall-parallel plane showing grid used in hemispherical bump simulation. Note that the grid is refined in the region where the flow is transitional and is coarse where the flow remains laminar.

million elements and the same for Mach 5.26 contained 40 million elements. The number of grid points in the y direction for $M_\infty = 3.37$ is shown in figure 8. Note that the fine grid contains 70 points within the height of the roughness.

All of the mean statistics reported in this paper have been checked for statistical convergence using over 20 000 samples spanning more than 160 D/u_∞ time units (where one domain flow through time is 50 D/u_∞). We first describe the grid spacings for $M_\infty = 3.37$ in the region downstream of the roughness to show how the fine grid resolution was arrived at. Here Δz was 0.0133, 0.033 and 0.066 and Δy_{min} was 0.0008, 0.001 and 0.01 for the fine, medium and coarse grids, respectively. At $x = 5$, Δx was 0.02, 0.049 and 0.07 for the fine, medium and coarse grids while at $x = 15$, it was 0.02, 0.09 and 0.11, respectively. We have attached the effect of grid resolution at $x = 5$, 15 and 25 and $z = 0$ and 1 in figures 9–10. The results indicate that the variation of the solution with the different grids is small indicating grid convergence. The differences between the grids is more prominent in the turbulent kinetic energy $TKE = \overline{u_i' u_i'}$ profiles when compared with u and ρ. Figure 11 shows the streamwise velocity contours for the three grids in the $y = 0.05$ plane to depict the small scales captured by the grids. Note that the difference in length scales captured by the medium to coarse grids is more prominent when compared with that captured by the fine to medium grids. The difference between the grids is more prominent in the van Driest transformed velocity (defined in § 6) in figure 12 where the coarse grid is clearly inadequate owing to its coarse Δy^+_{min} resolution while the agreement between the finer grids is good.

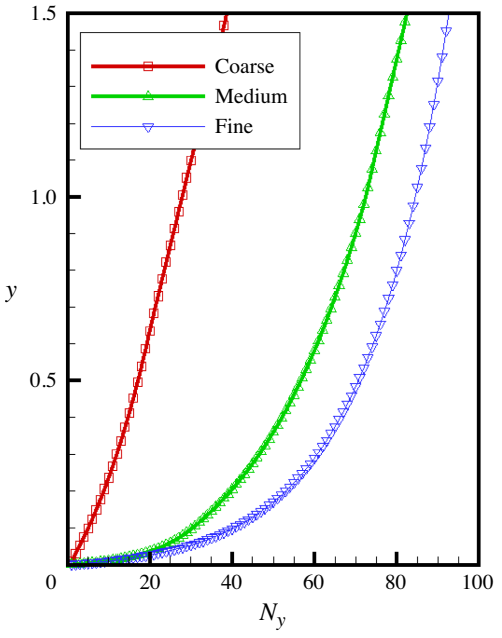

FIGURE 8. (Colour online) The number of grid points in the y direction for the three grids used for $M_\infty = 3.37$.

5. Qualitative comparison to experiment

Figure 13 shows the experimental planar laser-induced fluorescence (PLIF) images from Danehy *et al.* (2009) and instantaneous density and temperature contours in the symmetry plane from the computations. Note that the lower Mach number boundary layers undergo transition, while the Mach 8.23 flow remains laminar downstream of the roughness. Also the Mach 3.37 flow undergoes transition closer to the bump when compared with Mach 5.23. This trend is consistent between the experiment and our computation thereby serving as a qualitative validation of the nature of flow field downstream of the roughness. Note that the experimental and simulation figures are not exactly to scale although the downstream distance of the two are matched. The upstream boundary layer is thinnest for the lowest Mach number and, hence, if the boundary-layer thickness is taken as the relevant length scale, the bump is tallest for Mach 3.37. It is known in incompressible flows (Tani *et al.* 1962) that a larger roughness height (Re_k) moves the transition location closer to roughness and the observations made here are consistent for Mach 3.37 and 5.26. It has been observed that in general, higher Mach numbers stabilize the flow as seen by Danehy *et al.* (2007, 2009) and Chang & Choudhari (2009) and this trend is consistent with the present observations.

Figure 14 shows instantaneous temperature contours in a wall-parallel plane 1 mm from the flat plate for Mach 3.37 and 5.26 from DNS along with PLIF visualization for Mach 4.23 from Danehy *et al.* (2009). The unsteady flow features appear qualitatively similar between computation and experiment although the flow conditions are slightly different. For all three cases, it can be seen that unsteady flow features appear both close to the centreline and 1–2D on either side of the roughness separated by a region of relatively quiescent flow.

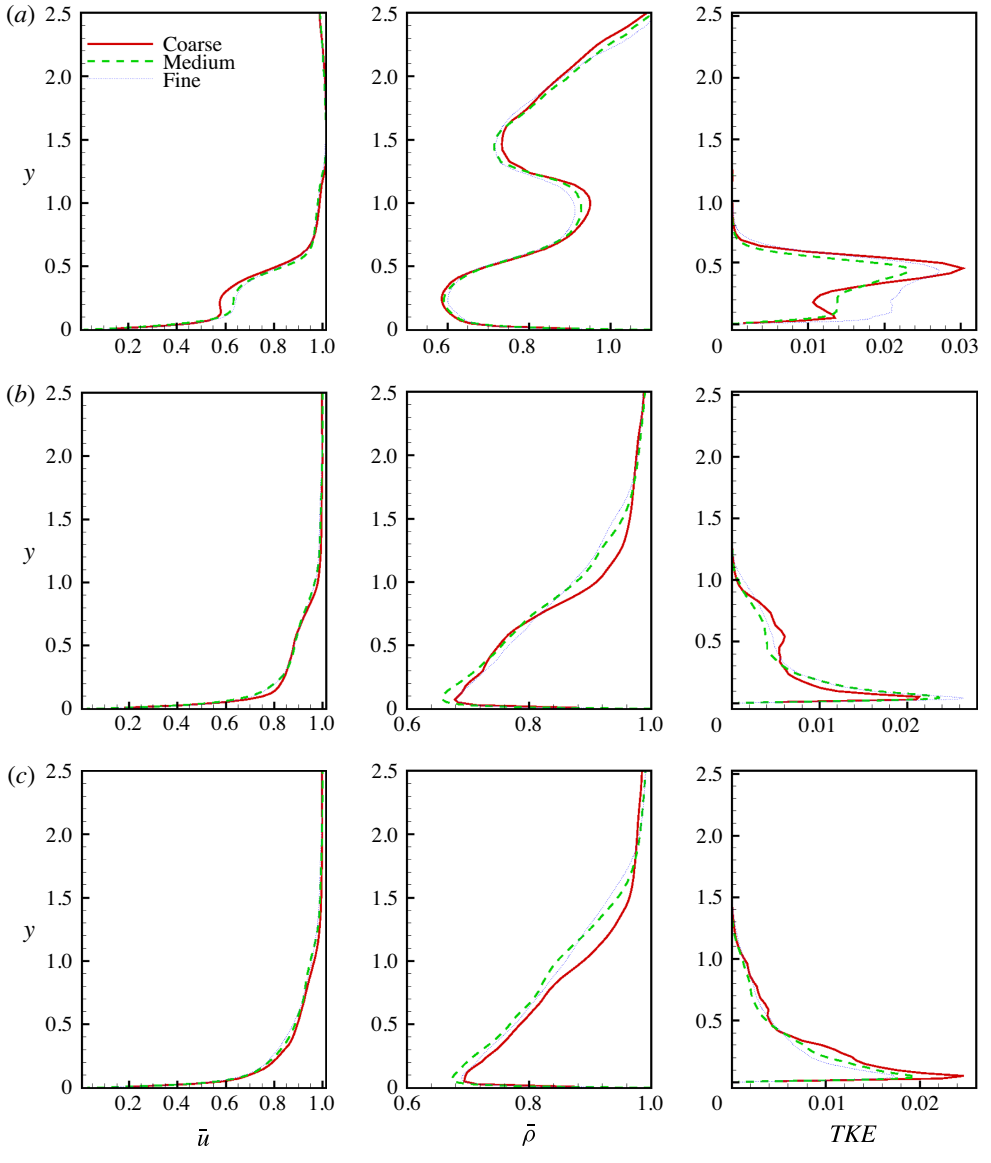

FIGURE 9. (Colour online) Results from grid convergence study. Profiles of mean streamwise velocity ($\overline{u}$), density ($\overline{\rho}$) and turbulent kinetic energy ($TKE = \overline{u_i' u_i'}$) with y at three streamwise stations: $x = 5$ (a), $x = 15$ (b) and $x = 25$ (c) in the symmetry plane ($z = 0$) are shown for $M_\infty = 3.37$.

6. Results

The results of the hemispherical bump simulations are discussed. Section 6.1 discusses the nature of the upstream separation induced by the roughness. Section 6.2 considers the formation of counter-rotating streamwise vortices downstream of the roughness; their perturbation of the separation shear layer is discussed in § 6.3. The various sources of unsteadiness that might induce transition are identified in § 6.4. Section 6.5 illustrates the formation of hairpin vortices behind the roughness. The

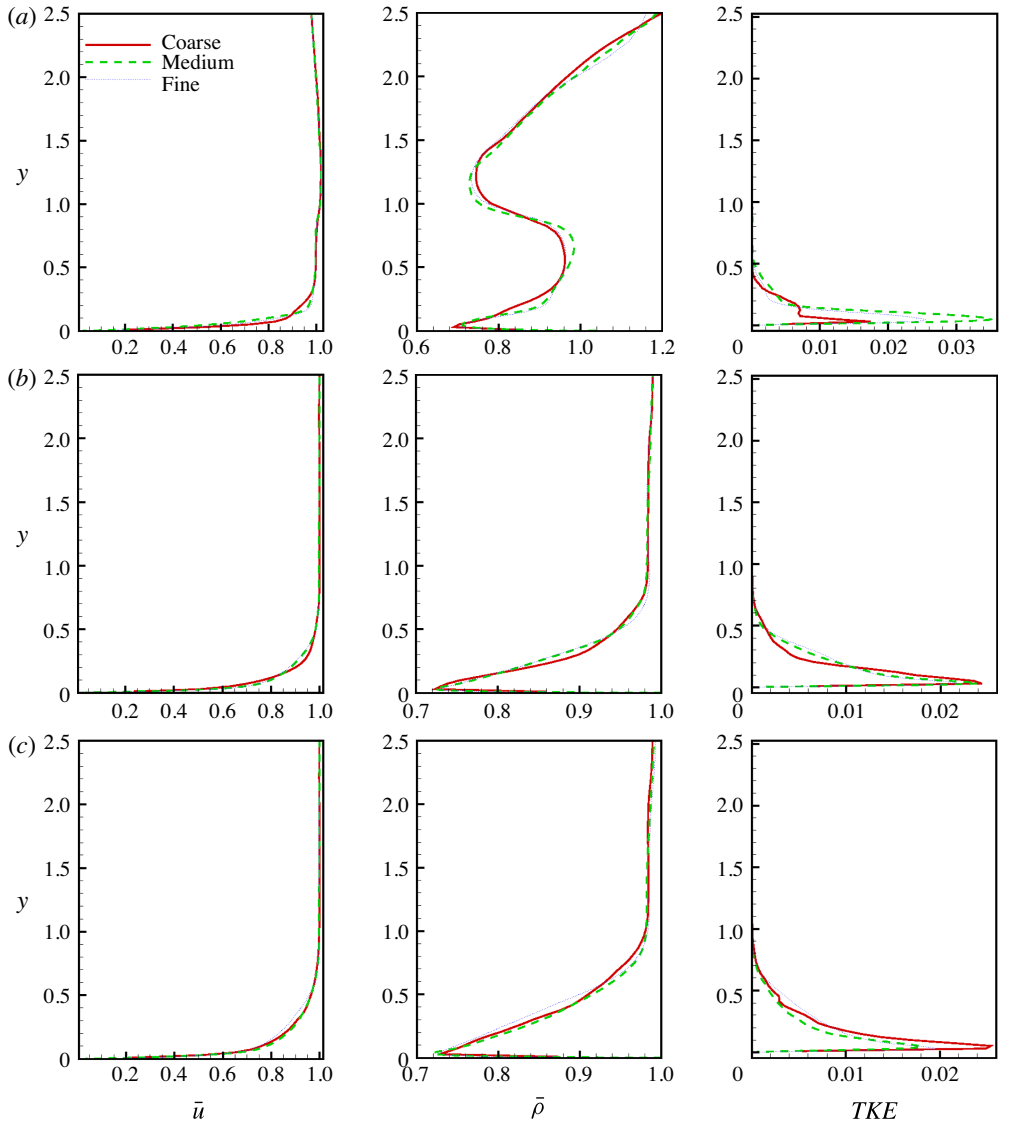

FIGURE 10. (Colour online) Results from grid convergence study. Profiles of mean streamwise velocity ($\overline{u}$), density ($\overline{\rho}$) and turbulent kinetic energy ($TKE = \overline{u_i' u_i'}$) with y at three streamwise stations: $x = 5$ (*a–c*), $x = 15$ (*d–f*) and $x = 25$ (*g–i*) in the $z = 1$ plane are shown for $M_\infty = 3.37$.

dominant frequencies in the flow for Mach 3.37 are discussed in § 6.6 and the mean flow is quantified in § 6.7. Finally, a local Reynolds number indicative of the trend of transition is computed in § 6.8.

6.1. *Upstream separation*

A laminar boundary layer undergoes three-dimensional separation upstream of a roughness element in its path. This separation results in the concentration of vorticity from the boundary layer into discrete spanwise vortices. This phenomenon has been

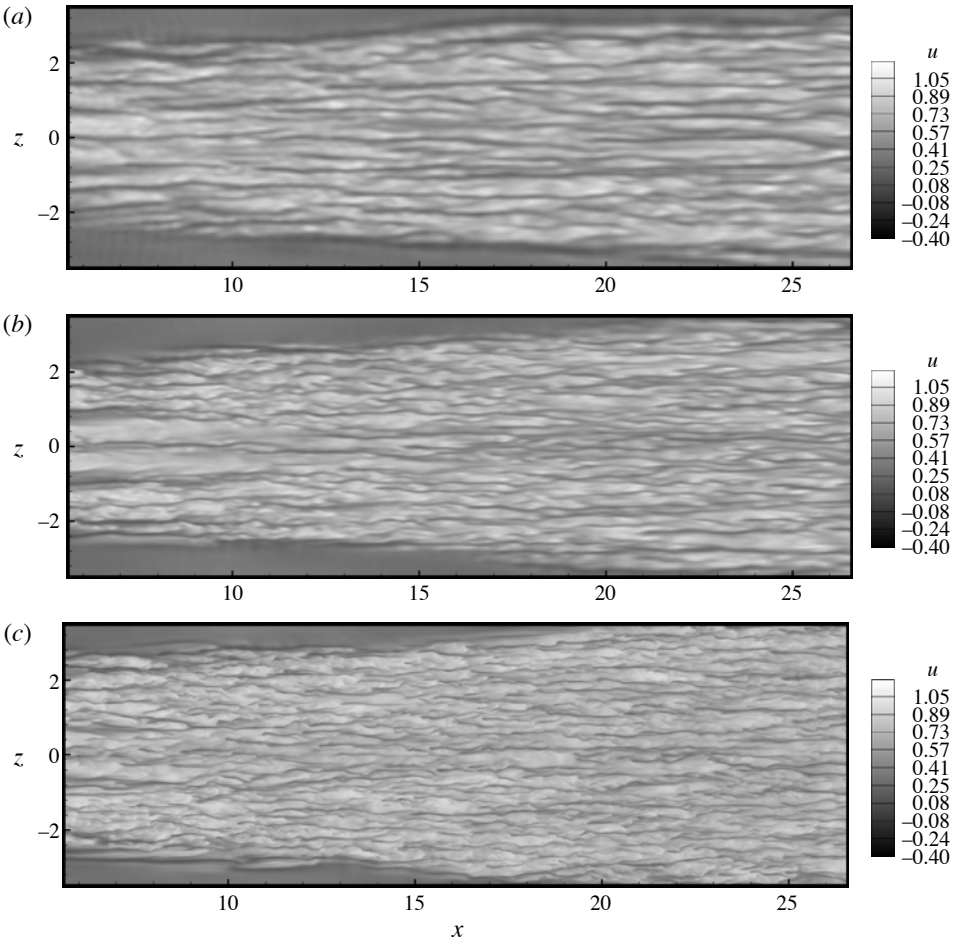

FIGURE 11. Streamwise velocity contours at $y = 0.05$ showing the effect of grid resolution for the coarse (a), medium (b) and fine (c) grids.

observed by various researchers including Baker (1979) and Simpson (2001). The number of vortices depends on the Mach number, Reynolds number and the height of the roughness. For incompressible flow past a cylinder placed on a flat plate, Baker (1979) presents a chart showing the effect of D/δ^* (where δ^* is the displacement thickness) and Re_D on the number of vortices formed upstream. Higher values of Re_D and D/δ^* were likely to produce an unsteady six-vortex system while lower values were likely to produce steady six-, four- or two-vortex systems, respectively. Table 2 lists the flow parameters and number of vortices observed in our simulations. Figure 15 shows the vortex system upstream of the roughness. A six-vortex system is produced for the Mach 3.37 and 5.26 flows, while a four-vortex system is produced for the Mach 8.23 flow. Since the vortices are highly unsteady for the Mach 3.37 flow, the number of vortices observed at a particular time instant may vary which is indeed the case in figure 15. The six-vortex system can be seen clearly in figure 16.

The six-vortex system is highly unsteady for the Mach 3.37 flow. Figure 16 shows the vortices formed upstream of the bump in the symmetry plane for the

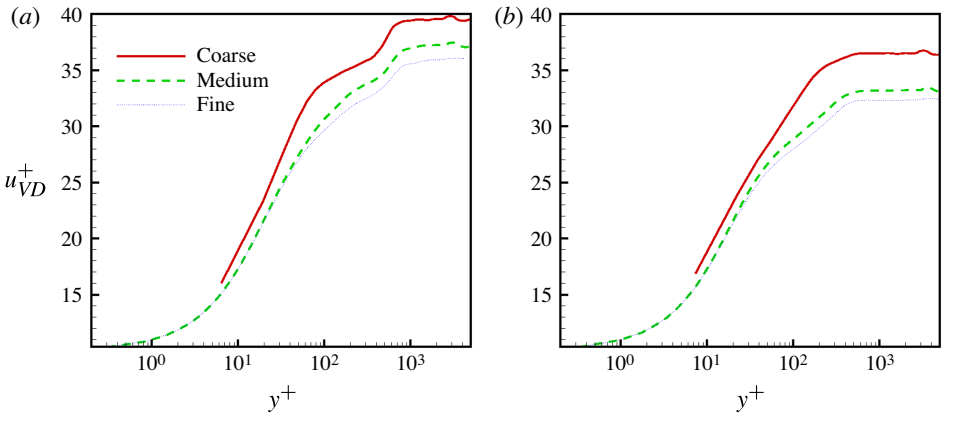

FIGURE 12. (Colour online) Effect of grid resolution on Van-driest transformed velocity at $x = 15$ and $z = 0$ (a) and 1 (b) for $M_\infty = 3.37$.

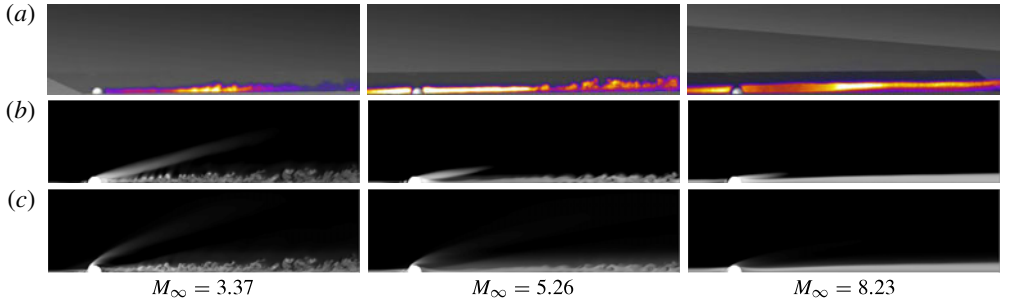

FIGURE 13. (Colour online) Experimental nitric oxide (NO)-PLIF images from Danehy *et al.* (2009) (a) with instantaneous density (b) and temperature (c) contours from simulation for $M_\infty = 3.37$, 5.26 and 8.23, respectively. Note that the qualitative trend of transition is consistent between experiment and simulation.

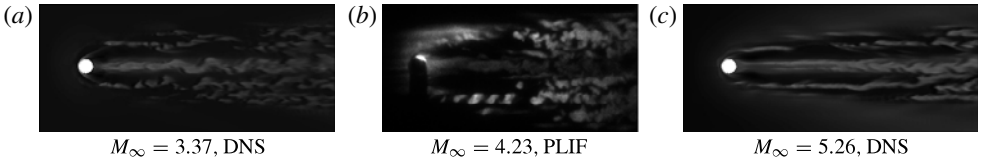

FIGURE 14. Instantaneous temperature contours from simulation for Mach 3.37 (a) and Mach 5.26 (c) compared with PLIF image for Mach 4.23 from Danehy *et al.* (2009) for qualitative purposes. Note the similarity in the unsteady features downstream.

Mach 3.37 flow where both instantaneous and mean streamlines are shown to depict the vortices. Note that the number of vortices differ in the instantaneous and mean, indicating the unsteady nature of the separation. To quantify the effect of separation, the skin-friction coefficient ($C_f = \tau_{wall}/0.5\rho_\infty u_\infty^2$) and Stanton number ($C_h = k(\partial T/\partial y)|_{wall}/\rho_\infty u_\infty C_p|T_w - T_\infty|$) are shown for the Mach 3.37 flow in the

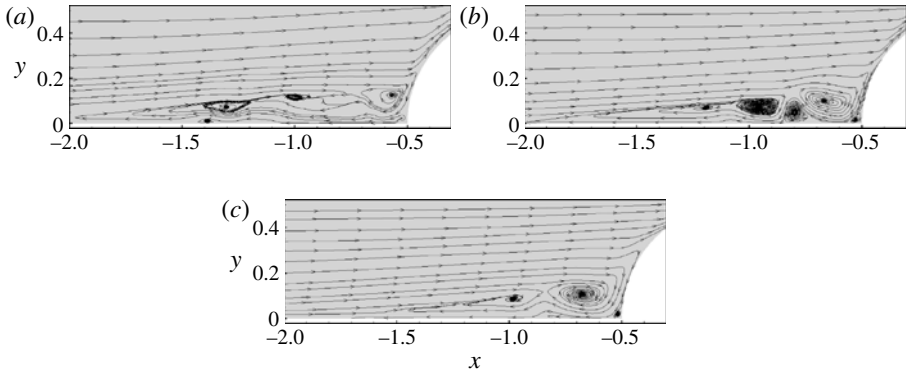

FIGURE 15. Instantaneous streamlines for Mach 3.37 (*a*), Mach 5.26 (*b*) and Mach 8.23 (*c*) indicating the number of vortices formed upstream.

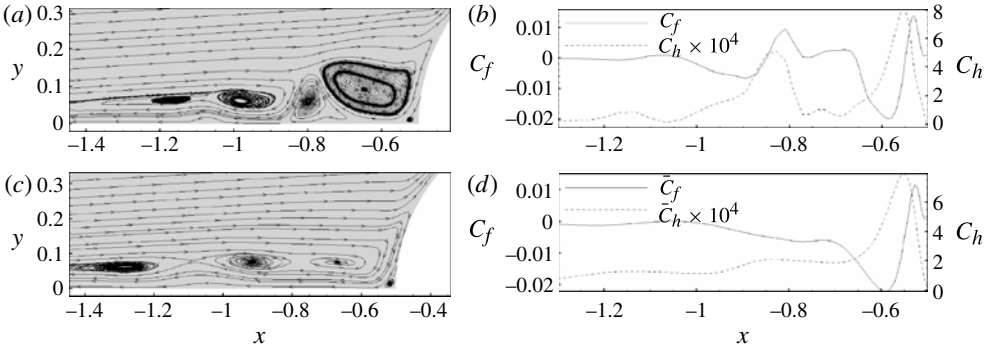

FIGURE 16. Streamlines (*a,c*) and C_f and C_h variation (*b,d*) for Mach 3.37 with instantaneous (*a,b*) and mean (*c,d*) plots indicating the highly unsteady nature of the flow.

M_∞	$Re_D = \dfrac{u_\infty D}{\nu_\infty}$	D/δ^*	Number of vortices
3.37	18 241	11.51	6 (highly unsteady)
5.26	28 378	6.44	6
8.23	33 662	2.92	4

TABLE 2. Parameters describing upstream separation.

symmetry plane in figure 16. Both instantaneous and mean values are plotted. The effect of counter-rotating vortices can be seen observed in the change in sign in C_f in the instantaneous curve. The vortices closest to the roughness appear to be strongest and cause a significantly higher C_f and C_h than the laminar values in its vicinity. The vortex present at $x = -15.8$ is unsteady and does not appear in the mean. Note that regions of high C_f occur close to the centre of the vortices while regions of high C_h occur in regions between two vortices.

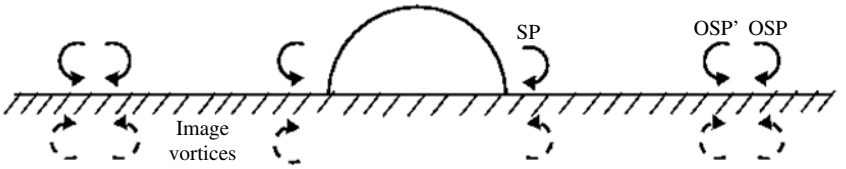

FIGURE 17. Schematic showing the nomenclature used for streamwise vortices (SP: symmetry plane; OSP: off-symmetry plane) at $x = 0$ in the y–z plane. Also shown are image vortices which induce w velocity to the vortices.

6.2. *Counter-rotating streamwise vortices*

The spanwise vortices formed upstream wrap around the roughness to give rise to streamwise vortices downstream of the roughness. Figure 17 shows a schematic of the streamwise vortices observed in a streamwise plane at the centre of the roughness. Very close to the roughness, there is a vortex (SP) which with increasing downstream distance would move closer to the symmetry plane due to the induced velocity by the image vortex and the low-pressure region created behind the roughness. Therefore, one vortex from both sides of the roughness moves closer to the symmetry plane giving rise to a counter-rotating vortex pair. These are referred to as the symmetry plane vortices (SP). Away from the symmetry plane, counter-rotating vortex pair(s) are formed which are the continuation of the vortex tubes from upstream. These are referred to as the off-symmetry plane vortices (OSP). Thus, downstream of the roughness, there exist counter-rotating SP and OSP vortices.

The counter-rotating vortices may be oriented so as to have an upwash or downwash between them. This depends on the flow conditions and the relative strength of the vortices upstream. When the vortices have an upwash, the effect of the mirror vortices is to induce them to move towards each other thus strengthening the magnitude of the vertical velocity between them. On the other hand, for vortices with a central downwash, the effect of the mirror vortices is to move the vortices away from each other; in effect weakening the velocity induced between them. Based on this reasoning, counter-rotating vortices with a central upwash close to the wall are more likely to induce transition as compared to those with a central downwash.

Figure 18 shows the instantaneous ω_x contours and streamlines at a streamwise plane in the centre of the roughness to illustrate the nature of the streamwise vortices. The number of vortices is higher for Mach 3.37 and 5.26 due to the higher number of upstream vortices. Also, the spanwise location of the OSP vortices for Mach 3.37 oscillates with time due to the highly unsteady upstream vortices. Transient growth theory predicts that streamwise vortices are optimal disturbances for boundary layers. The streamwise vortices predicted by transient growth are counter-rotating and equal in strength. However, the OSP vortices created by the roughness element differ in the following respects: (i) vortices with positive ω_x have their centre located closer to the wall as compared with the vortices with negative ω_x and thus the line joining the centre of the vortices is at an angle to the wall; (ii) the size and strength of the counter-rotating vortices is noticeably different; (iii) they are not periodic in the span.

Table 3 lists the magnitude of the streamwise vorticity at the centre of the respective vortices whose nomenclature is based on the schematic in figure 17. The maximum ω_z listed is for an unperturbed boundary layer at the location of the roughness. From table 3, the strength of the streamwise vortices is higher for a higher spanwise vorticity from the unperturbed boundary layer and thus is highest for Mach 3.37 and lowest for

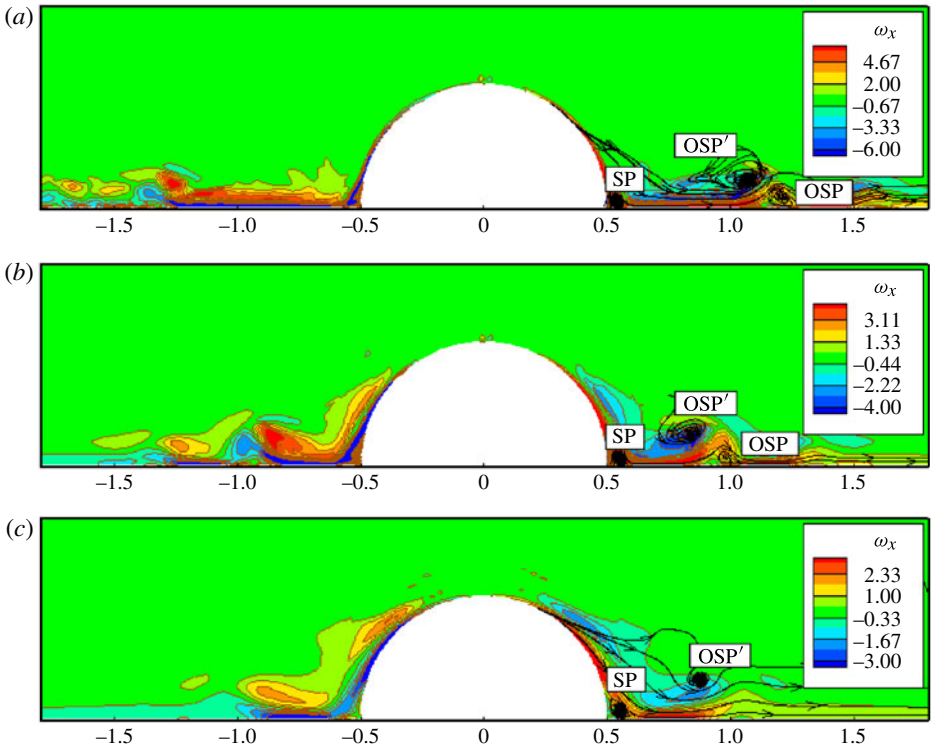

FIGURE 18. (Colour online) Contours of instantaneous ω_x along with contour lines (shown in brown online) and instantaneous streamlines (black) for Mach 3.37 (*a*), 5.26 (*b*) and 8.23 (*c*) depicting the streamwise vortices at $x = 0$ in the y–z plane.

M_∞	$\omega_{x,SP}$	$\omega_{x,OSP}$	$\omega_{x,OSP'}$	$\omega_{z,max}$
3.37	9.6	−5.4	3.6	−4.5
5.26	5.9	−5.1	1.7	−3.0
8.23	1.7	−1.1	–	−1.5

TABLE 3. The strength of the streamwise vortices at $x = 0$ depicted in figure 18.

Mach 8.23. Note that the strength of the vortices decreases with increasing distance from the roughness element. The SP vortices are the strongest of the vortices, hence implying a higher likelihood of the flow breaking down in the symmetry plane.

6.3. *Perturbation of shear layer*

The boundary layer separates on either side and downstream of the roughness element creating a separated shear layer which is shown in figure 19 for Mach 3.37. Far upstream, it can be seen that the boundary layer is attached and two-dimensional. The spanwise extent of the shear layer depends on the upstream separation length. At the centre of the roughness ($x = -15$), the smaller SP vortex forms away from the shear

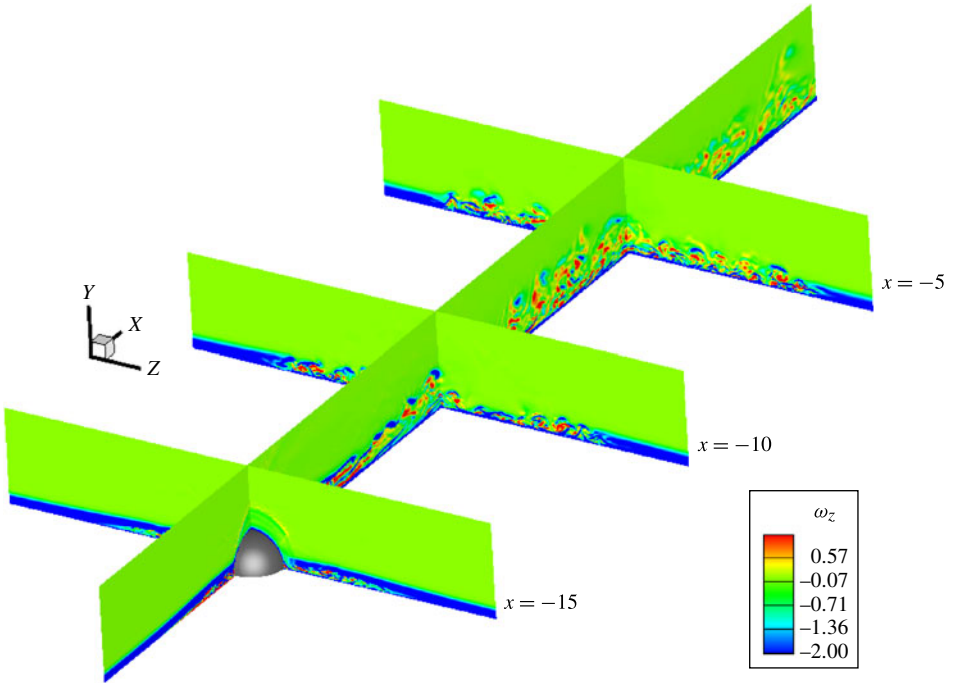

FIGURE 19. (Colour online) The separation shear layer formed due to the roughness using contours of spanwise vorticity for Mach 3.37 flow.

layer while the larger OSP vortices are in contact with the shear layer. Downstream of the roughness, this shear layer in the symmetry plane is close to the SP vortices.

The counter-rotating SP and OSP vortices perturb the shear layer in their vicinity. The size, strength and magnitude of unsteadiness of the vortices determines the nature of the perturbation to the shear layer; the receptivity and stability characteristics of the shear layer determines whether or not the flow undergoes transition. Note that these perturbations are inhomogeneous in the span and therefore biglobal stability theory (Groskopf *et al.* 2008; Choudhari *et al.* 2010) could lead to a better understanding of the instability mechanisms associated with such flows. From figure 19, it can be seen that the flow breaks down downstream of the roughness both at and away from the symmetry plane.

It is known at low speeds that a uniform shear flow past a sphere sheds hairpin-shaped vortices (Sakamoto & Haniu 1995). Also, Acarlar & Smith (1987) observed that hairpin vortices form behind a teardrop-shaped obstacle placed on a flat plate at incompressible speeds even though the horseshoe vortices around the obstacle are absent. To assess whether such shedding takes place in the current simulations, we perform a two-dimensional simulation past a semicircular hump with identical free-stream and wall conditions of the Mach 3.37 boundary layer. We also perform a two-dimensional incompressible simulation with the same Re_D as Mach 3.37 to assess any effect of compressibility. The shear layer downstream of the roughness for the two-dimensional cases is shown along with the symmetry plane shear layer from the three-dimensional simulation in figure 20. Although some unsteadiness was observed in the two-dimensional Mach 3.37 flow downstream, the shear layer re-attaches with the flat plate without breaking down, in contrast to the three-dimensional

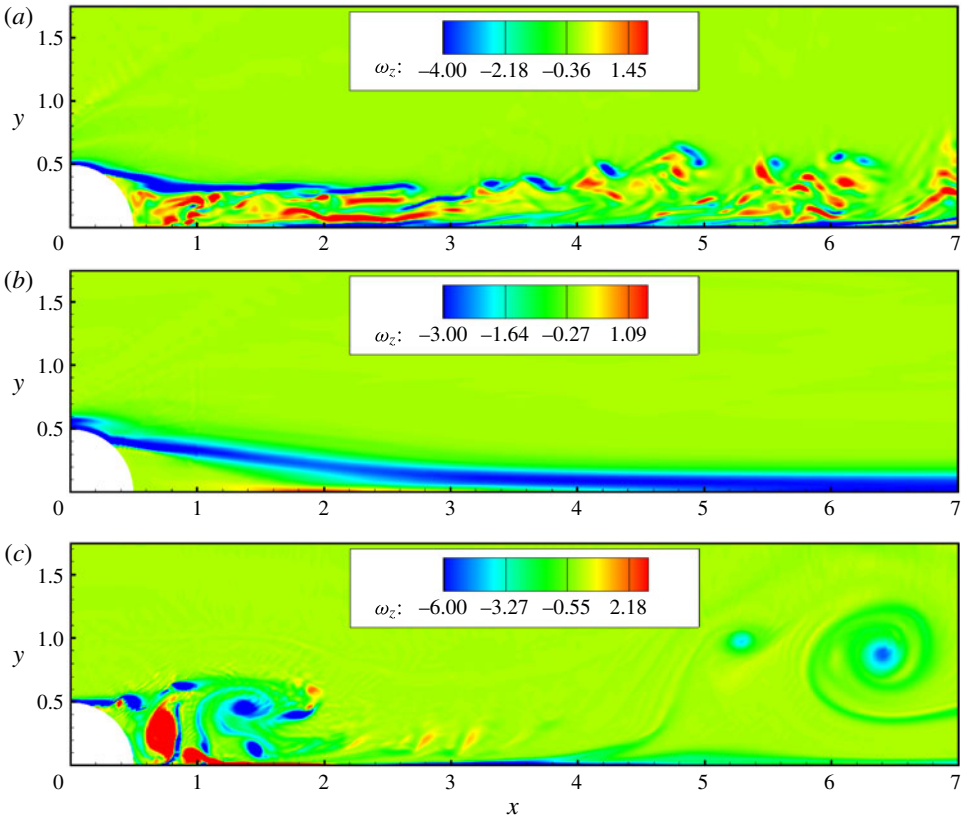

FIGURE 20. (Colour online) Contours of instantaneous ω_z for symmetry plane three-dimensional simulation (*a*), Mach 3.37 two-dimensional simulation (*b*) and incompressible two-dimensional simulation (*c*).

case, where the shear layer breaks down due to the SP vortices. The incompressible two-dimensional simulation revealed that vortex shedding occurred downstream of the roughness similar to the shedding behind a bluff body. This indicates that the breakdown of the shear layer downstream of the bump in the three-dimensional flow is due to its perturbation by the streamwise vortices below it. The absence of vortex shedding at supersonic speeds was also observed by Chang & Choudhari (2009) who performed a parametric study of the effect of two-dimensional roughness on a flat plate at subsonic and supersonic speeds and subcritical Reynolds numbers. They conclude that the absolute vortex-shedding process was weak at supersonic speeds and hence convective instabilities might become more dominant at high speeds.

6.4. *Sources of unsteadiness*

When a laminar supersonic boundary layer interacts with a roughness element, possible sources of unsteadiness are due to the unsteady vortex system upstream, shock-induced unsteadiness and shear layer instability. In § 6.1, it was seen that the Mach 3.37 flow was highly unsteady upstream. The unsteadiness is also observed in incompressible flows (see e.g. Baker 1979) and depends on Reynolds number. The upstream separation region with discrete counter-rotating vortices becomes unstable beyond a critical *Re* and becomes unsteady. When the supersonic boundary layer

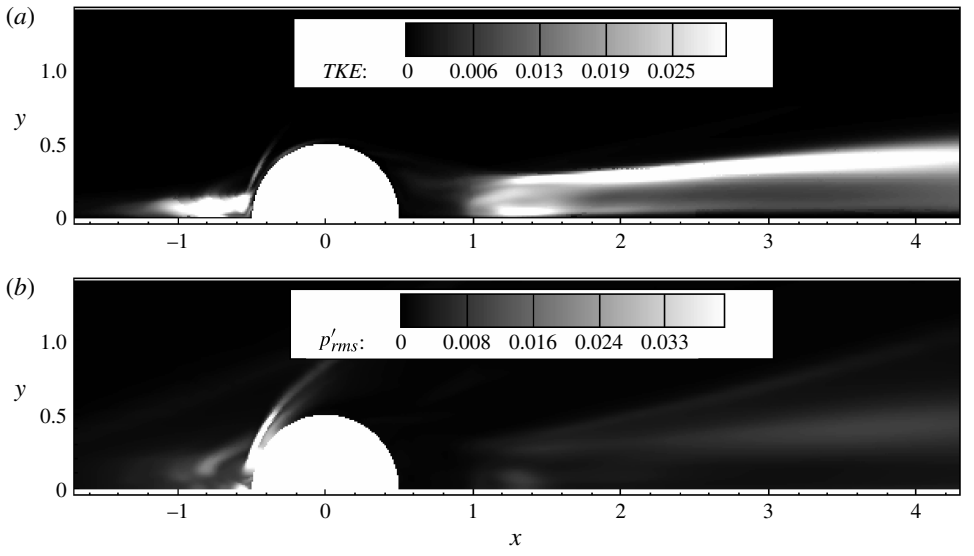

FIGURE 21. Sources of unsteadiness for Mach 3.37. $p'_{rms}/\bar{p}$ contours are shown to depict shock-induced unsteadiness (*a*). Here turbulent kinetic energy (*TKE*) contours are shown in the symmetry plane (*b*) to depict the unsteadiness due to the vortices and shear layer.

comes in contact with the roughness element, a shock wave is produced at the wall-normal location corresponding to the sonic line. This shock which is inherently unsteady, could potentially perturb the flow in the vicinity of the roughness element thereby causing the flow to become unstable. As described in § 6.3, a three-dimensional separation shear layer is formed. Streamwise vortices exist below both the shear layers and act as a perturbation. Also, the shear layer contains inflexion points in its mean profile and is susceptible to the inviscid Kelvin–Helmholtz instability. Depending on the Mach number and Reynolds number, the shear layer could become unstable.

One or more of the above factors can cause the flow to break down and undergo transition. Figure 21 illustrates the above sources of unsteadiness for the Mach 3.37 flow. Note the p'_{rms} is highest at the shock location upstream while the turbulent kinetic energy ($TKE = \overline{u'_i u'_i}/u_\infty^2$) is highest in the vortex system upstream and the shear layer downstream. The p'_{rms} contour suggests that the secondary shocks formed downstream of the roughness are relatively weak and thus are less likely to contribute to transition of the flow.

Figure 22 shows the wall-normal variation of the turbulent kinetic energy (*TKE*) in the symmetry plane for the three flows. Three upstream and downstream locations are selected whose distance from the roughness is indicated in the figure. Upstream of the roughness, the Mach 3.37 flow is highly unsteady, while the higher Mach number flows are nearly steady. The maximum unsteadiness for Mach 3.37 occurs $1D$ upstream of the bump indicating that it is due to the unsteady spanwise vortices. The maximum unsteadiness occurs closest to the bump for Mach 5.26 and 8.23 away from the wall suggesting that it is due to the shock produced by the roughness. Thus, we see that the shock-induced unsteadiness is weak for the cases considered whereas the unsteadiness from the vortex system is strong for Mach 3.37. Downstream of the

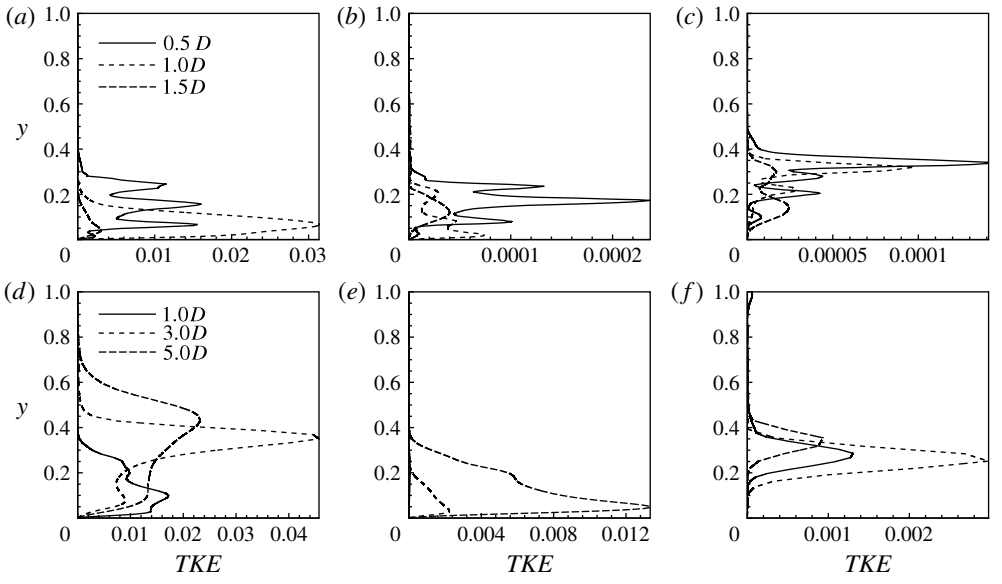

FIGURE 22. Wall-normal variation of turbulent kinetic energy (*TKE*) upstream (*a–c*) and downstream (*d–f*) of the bump for Mach 3.37 (*a,d*), 5.26 (*b,e*) and 8.23 (*c,f*) in the symmetry plane. Distance from the centre of the roughness is indicated in the figures.

M_∞	Unsteadiness in vortex system	Shock-induced unsteadiness	Shear layer unsteadiness
3.37	**Strong**	Weak	**Strong**
5.26	Weak	Weak	**Strong**
8.23	Weak	Weak	Weak

TABLE 4. The strength of unsteadiness based on the magnitude of turbulent kinetic energy (*TKE*) due to the different possible sources.

roughness, the unsteadiness is stronger than upstream for Mach 5.26 and 8.23 due to the perturbation of the shear layer by the streamwise vortices. For Mach 3.37 and 5.26, note that the unsteadiness increases with distance from the bump indicating the likelihood of transition further downstream. For Mach 8.23, the unsteadiness is an order of magnitude lower than the corresponding values for Mach 3.37 and 5.26 and decreases between 3*D* and 5*D* downstream indicating that the flow is stable to the perturbation of the shear layer. Thus, the unsteadiness due to the shear layer is strong for Mach 3.37 and 5.26 and weak for Mach 8.23.

Based on the observations from figure 22, we classify the unsteadiness from the three possible sources based on the magnitude of turbulent kinetic energy (*TKE*) in table 4. The shock-induced unsteadiness appears to be weak for all the three cases. For Mach 3.37, where the flow transitions closest to the roughness, the unsteadiness in both the upstream vortex system and the shear layer downstream are strong. In contrast, for Mach 5.26, the upstream vortices are nearly steady while the shear layer appears to be unstable, leading to larger levels of unsteadiness downstream. For

Mach 8.23, the unsteadiness is weak both in the upstream separation region and in the shear layer downstream.

6.5. *Hairpin-shaped vortices*

Transition is characterized by the prominent presence of hairpin vortices. Recall that the SP and OSP vortices perturb the separation shear layer, and for Mach 3.37 and 5.26, the shear layers are unstable and break down. The shear layer can be visualized as lines of vorticity. The counter-rotating streamwise vortices have an upwash or downwash at their centre depending on their direction of rotation, and can be visualized using the Q criterion (Hunt, Wray & Moin 1988):

$$Q = -0.5\frac{\partial u_i}{\partial x_j}\frac{\partial u_j}{\partial x_i}. \tag{6.1}$$

Figure 23 visualizes the streamwise vortices and shear layer for all three Mach numbers. Note that the vortex lines are perturbed at spanwise locations corresponding to the streamwise vortices. For Mach 3.37 and 5.26, the counter-rotating vortices have an upwash causing the vortex lines to form hairpin-shaped loops. For Mach 3.37, one such loop is formed at the symmetry plane and one on either side due to the OSP vortices. For Mach 5.26, two such loops are formed close to the symmetry plane with one on either side. For Mach 8.23, two pairs of counter-rotating vortices are formed close to the symmetry plane which have a downwash at each of their centres, respectively. As a result, inverted hairpin loops form on either side of the symmetry plane.

When the strength of the streamwise vortices is large enough, the hairpin loops break away to form coherent hairpin vortices. Figures 25–27 show isocontours of Q coloured by instantaneous streamwise velocity for Mach 3.37 and 5.26, respectively. Note the vortical fine scale structures created by the roughness and spreading of the turbulent wake. Even close to the outflow, coherent hairpin vortices are observed in what appears to be a visibly turbulent flow. Note that close to the outflow, the spanwise extent of the turbulent region is higher for Mach 3.37 as compared with Mach 5.26. The appearance of hairpin vortices is striking for both cases. Initially trains of hairpins are seen but with increasing downstream distance, they spread in the span giving rise to more such vortices and far downstream, the entire span is populated by such hairpins. Note that for Mach 5.26, the presence of hairpin vortices occurs farther away from the roughness when compared with Mach 3.37 and this is consistent with the experimental observations discussed in § 5. Such hairpin vortices have also been observed at incompressible speeds behind a hemispherical protuberance by Acarlar & Smith (1987) and Klebanoff *et al.* (1992). They also observe that with increasing downstream distance from the roughness, secondary vortices are formed and far downstream the flow resembles a turbulent boundary layer. The mean velocity profiles also closely match a canonical turbulent boundary layer profile indicating that the hairpin vortices caused the flow to transition to turbulence.

Note that the Mach 8.23 flow does not undergo transition, and the hairpin vortices are conspicuously absent. As in § 6.2, a downwash between the counter-rotating vortices implies a weakening of their effect due to their moving away from each other. Closer to the outflow for Mach 8.23, one vortex from either side of the symmetry plane moves closer to each other as to create an upwash between them. Although their strength has considerably decreased with increasing distance, it is therefore possible that the Mach 8.23 boundary layer might undergo transition at even larger distances downstream.

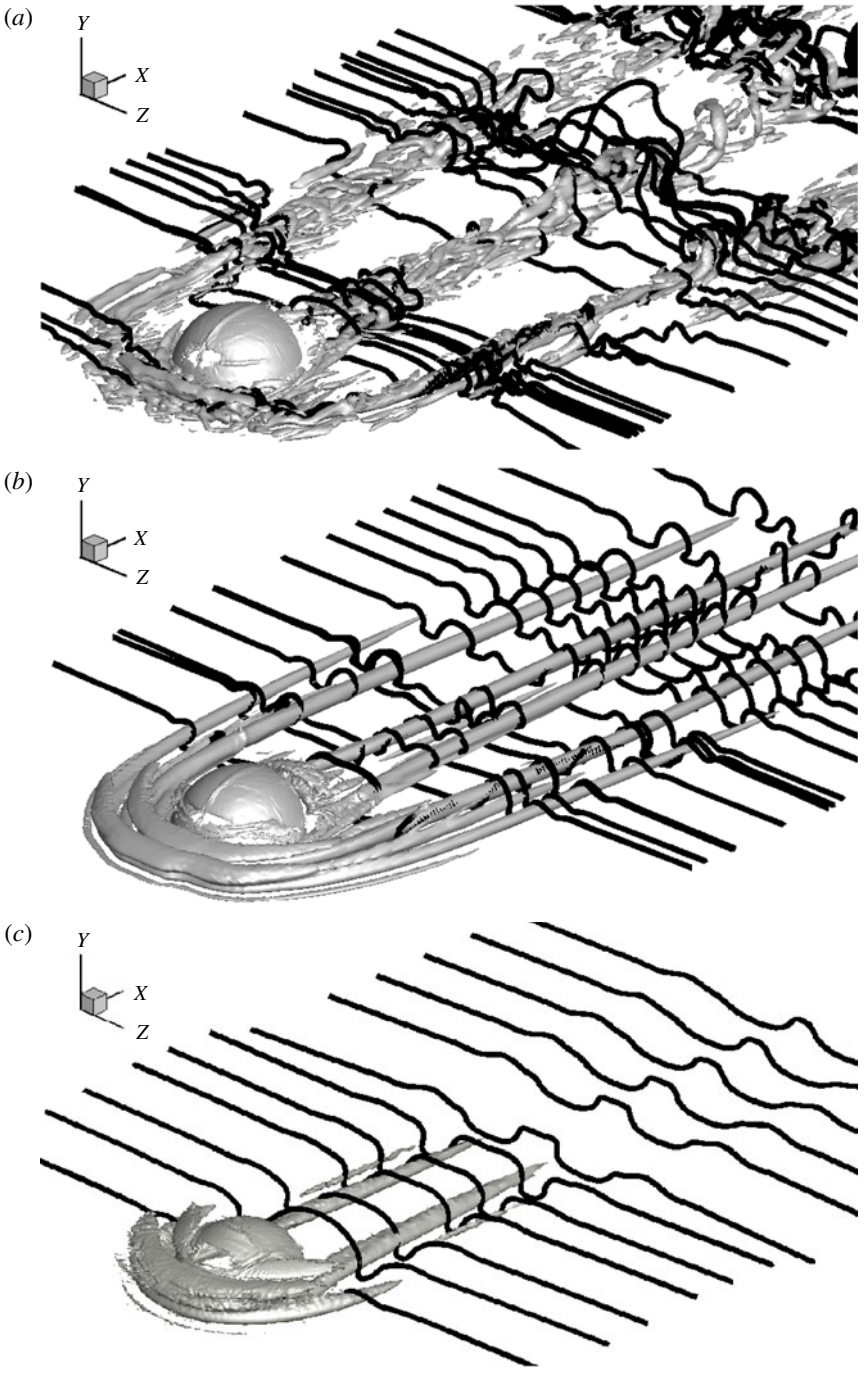

FIGURE 23. Isocontours of the Q criterion with instantaneous vortex lines for Mach 3.37 (a), 5.26 (b) and 8.23 (c).

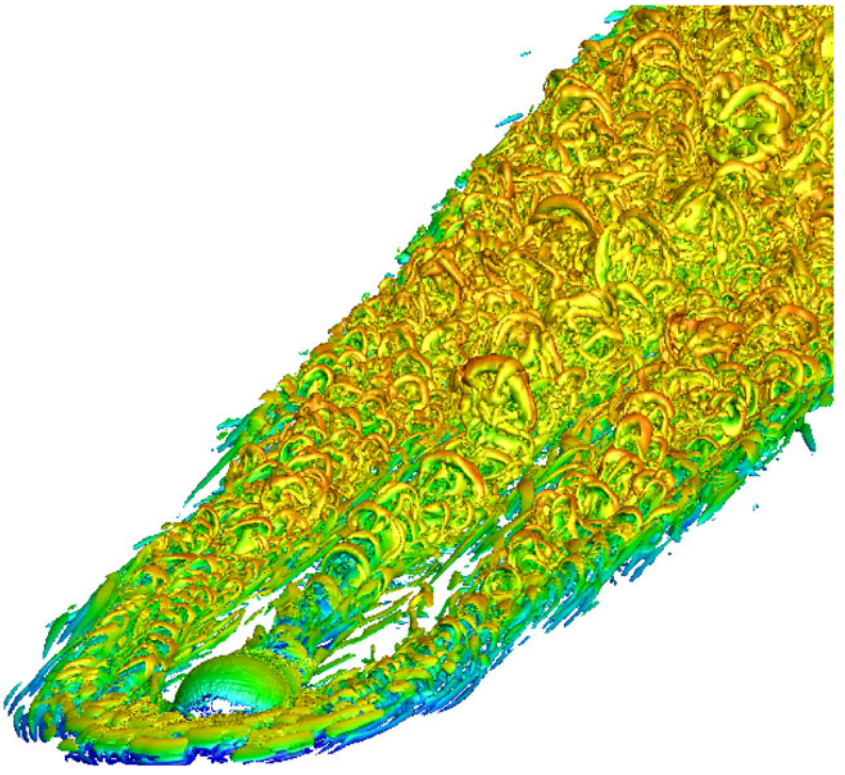

FIGURE 24. (Colour online) The $Q = 0.25$ isocontours coloured by streamwise velocity for Mach 3.37 depicting hairpin-shaped vortices.

6.6. *Temporal spectra for Mach 3.37*

Data were collected at locations both upstream and downstream of the roughness for Mach 3.37 to obtain the dominant frequencies in the flow. The data were collected over four domain flow through times, corresponding to an interval of $200D/u_\infty$. The spectra are reported at the points close to the wall except otherwise specified in the figures. The pressure signals 2–3D upstream of the roughness (figure 28) indicate a dominant Strouhal number ($St = fD/u_\infty$) of $St = 0.023$ corresponding to a dimensional frequency of $f = 8$ kHz based on $u_\infty = 1400$ m s^{-1} from the experiment. The $St = 0.023$ is prominent even $0.4D$ away from the symmetry plane. The streamwise location and the amplitude of the fluctuations suggest that this frequency is related to the first separation point of the boundary layer. The v velocity spectra (figure 28) showed that $St = 0.2$ is dominant 1 and 2D upstream of the roughness. This frequency is likely related to the unsteady vortex seen around $x = -16$ in figure 16. Note that closer to the roughness at $x = -16$, the spectra appear more broadband compared with that at $x = -17$.

Wall-pressure spectra are reported at different distances upstream of the roughness in the symmetry plane in figure 29. Also plotted are lines of slope -1 and -5 which have been observed in fully turbulent boundary layers by Choi & Moin (1990) in the incompressible regime and by Pirozzoli & Grasso (2006) and Beresh *et al.* (2011) in the supersonic regime. Note that the spectra appear broadband closer to the roughness indicating the highly unsteady nature of the upstream vortices. The maximum spectral

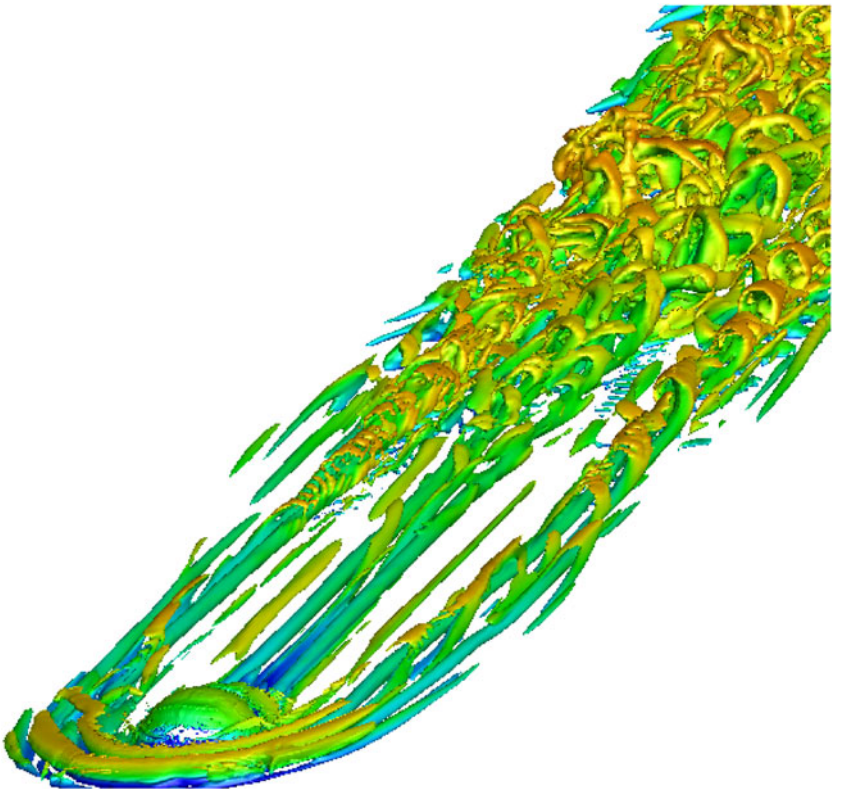

FIGURE 25. (Colour online) The $Q = 0.1$ isocontours coloured by streamwise velocity for Mach 5.26 depicting hairpin-shaped vortices.

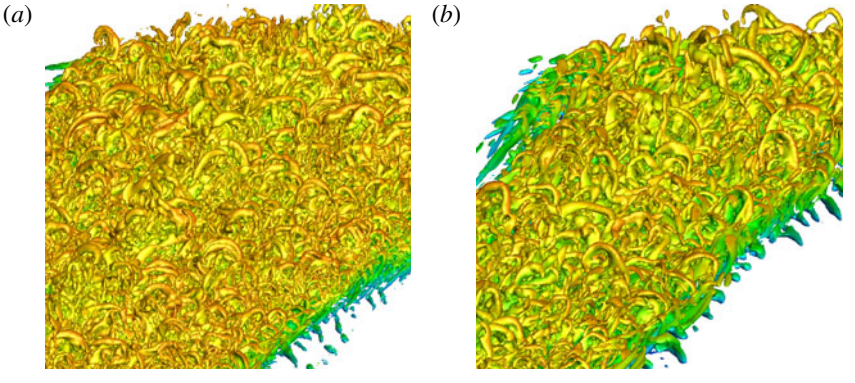

FIGURE 26. (Colour online) Hairpin vortices far downstream for Mach 3.37 (*a*) and Mach 5.26 (*b*). Here $Q = 0.25$ (*a*) and $Q = 0.1$ (*b*) coloured by streamwise velocity contours.

content occurs at $St < 0.2$ which showed up as a dominant peak in the v velocity spectra. Also shown in figure 29 are the wall-pressure spectra at points away from the symmetry plane at the centre of the roughness. The spectra again appear broadband

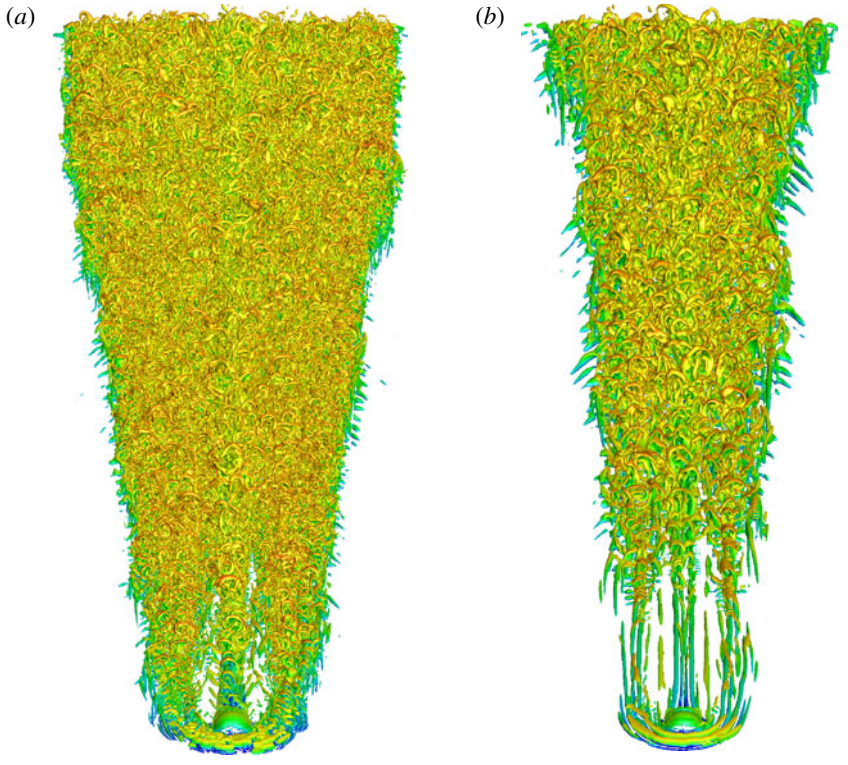

FIGURE 27. (Colour online) Top view of hairpin vortices for Mach 3.37 (*a*) and Mach 5.26 (*b*).

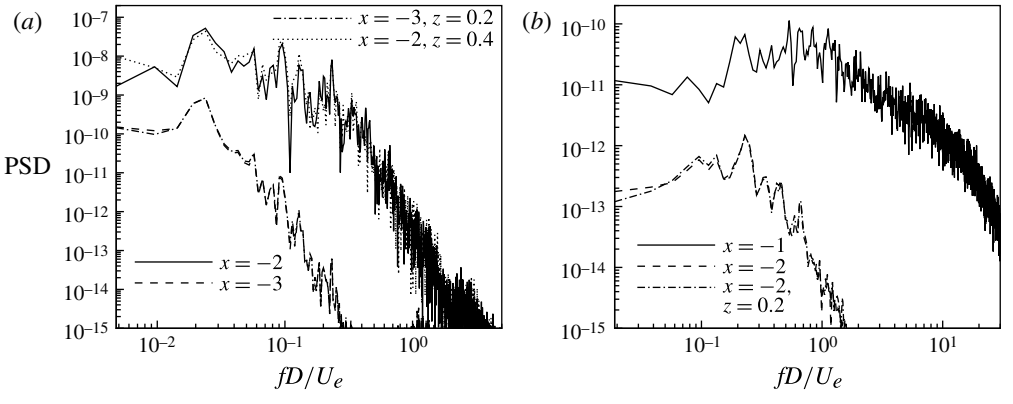

FIGURE 28. Temporal wall-pressure spectra (*a*) and *v* velocity spectra (*b*) for Mach 3.37.

as observed upstream but note that now the maximum spectral content occurs over a broader range of frequencies with $St < 1$.

The downstream evolution of the pressure spectra at the wall and at $0.5D$ from the wall is shown in figure 30. Note that beyond $x = 0$, the curves collapse onto a single curve at both wall-normal locations. The wall-pressure spectra far downstream

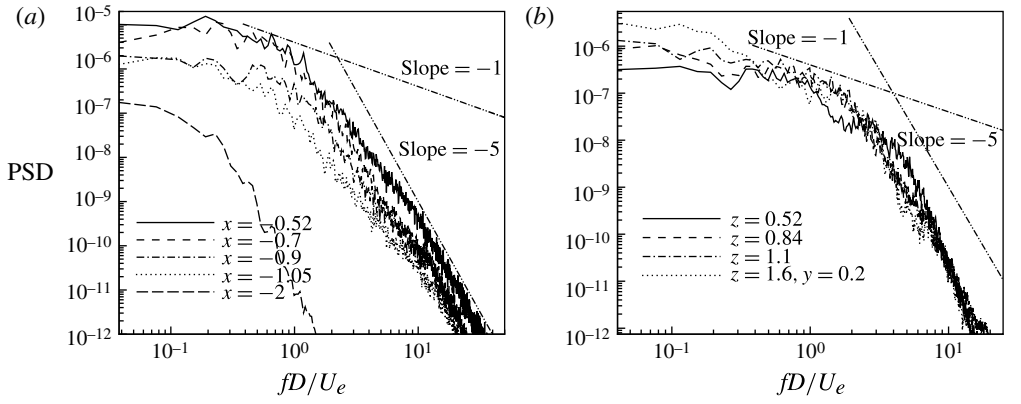

FIGURE 29. Temporal wall-pressure spectra showing variation with distance from the roughness in the symmetry plane (*a*) and in the streamwise plane at the centre of the roughness (*b*) for Mach 3.37.

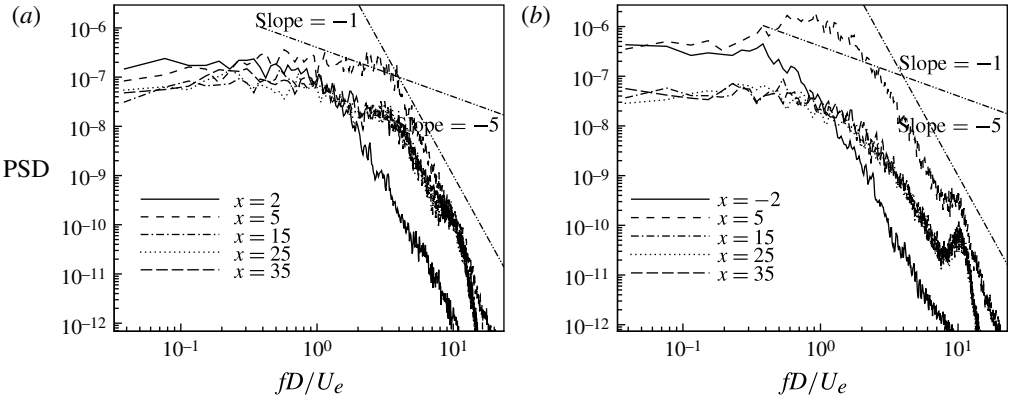

FIGURE 30. Temporal pressure spectra showing downstream evolution at the wall (*a*) and at $y = 0.5$ (*b*) for Mach 3.37.

indicates a distinct region with a slope of -1 and the curve flattens out for lower frequencies. This behaviour is also observed in Beresh *et al.* (2011) for fully turbulent boundary layers for higher Re_θ and suggests that the flow is turbulent with characteristics of a canonical turbulent boundary layer.

6.7. *Mean flow characteristics*

Mean Stanton number (C_h) contours are shown at the wall for all three Mach numbers in figure 31. As expected, transition causes higher C_h due to a larger temperature gradient at the wall. Immediately downstream of the roughness, streaks of higher C_h are observed for all three Mach numbers at locations corresponding to the streamwise vortices. The streamwise vortices transport higher-temperature fluid towards the wall and lower-temperature fluid away from the wall causing this increase in C_h. Note that since $T_{wall}/T_{aw} < 1$, the maximum temperature in the laminar boundary layer occurs away from the wall. For Mach 3.37, the hairpin vortices cause increased spanwise

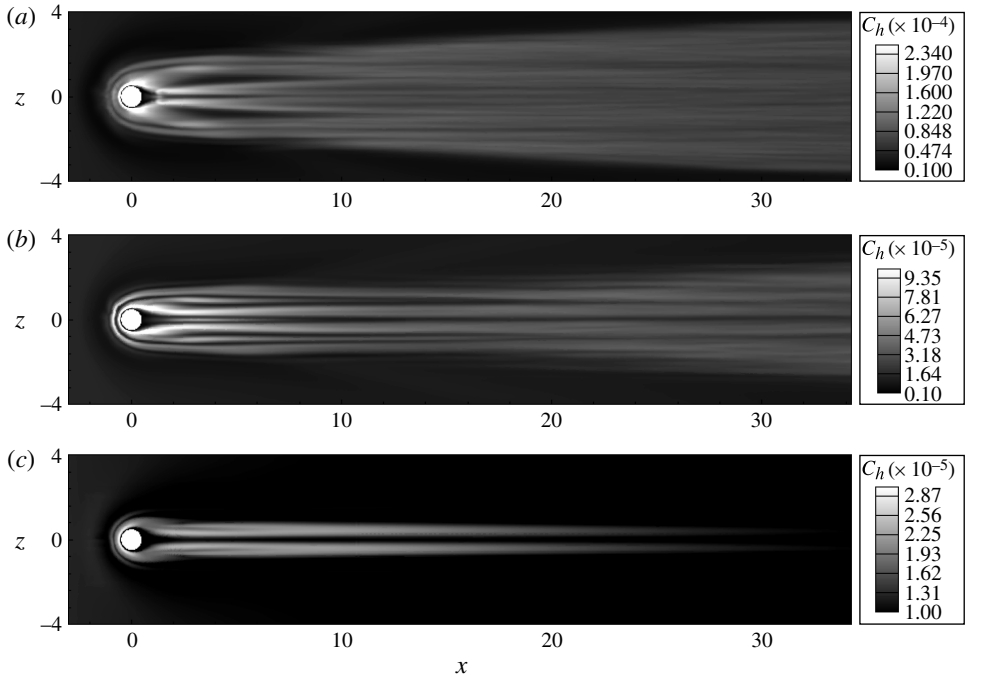

FIGURE 31. Stanton number (C_h) contours for Mach 3.37 (*a*), Mach 5.26 (*b*) and Mach 8.23 (*c*).

mixing of the flow which yields a larger region of high C_h beyond $x = -10$. With increasing downstream distance, it can be seen that the flow becomes more uniform in the span. Similar behaviour is observed for Mach 5.26. For Mach 8.23, a pair of high C_h streaks are formed whose strength decreases with increasing downstream distance consistent with the flow not transitioning.

Figure 32 shows the streamwise variation of mean C_f at $z = 0$, 0.5 and 1.0 from the symmetry plane for the three Mach number flows. Also plotted is the laminar C_f curve if the roughness were absent (obtained from a similarity solution) and a turbulent C_f curve if the boundary layer were turbulent from the leading edge of the flat plate. Upstream of the bump, the C_f matches the laminar value as expected. Close to the bump, the effect of upstream separation is seen where the C_f is negative. Immediately downstream of the bump, there is a significant rise in C_f for all three flows, which is attributed to both the presence of streamwise vortices which transport higher momentum fluid from above to the near-wall region and the acceleration of the mean flow as it moves towards the low-pressure region created downstream of the bump. Beyond the low-pressure region, the C_f decreases as expected.

For Mach 3.37, the C_f rises significantly above the laminar value and remains high indicating that the flow has transitioned. This location corresponds to the break up of the hairpins causing the flow to undergo transition. At $x = -10$, there is a significant spanwise variation in C_f but closer to the outflow, the C_f appear to converge to a single value. Note that Re_θ ranges from 1000 to 2400 and is significantly higher in the symmetry plane compared with other locations. This can be attributed to the upward deflection of the flow by the roughness element resulting in a higher boundary-layer thickness. For Mach 5.26, the flow begins to undergo transition beyond $x = 0$

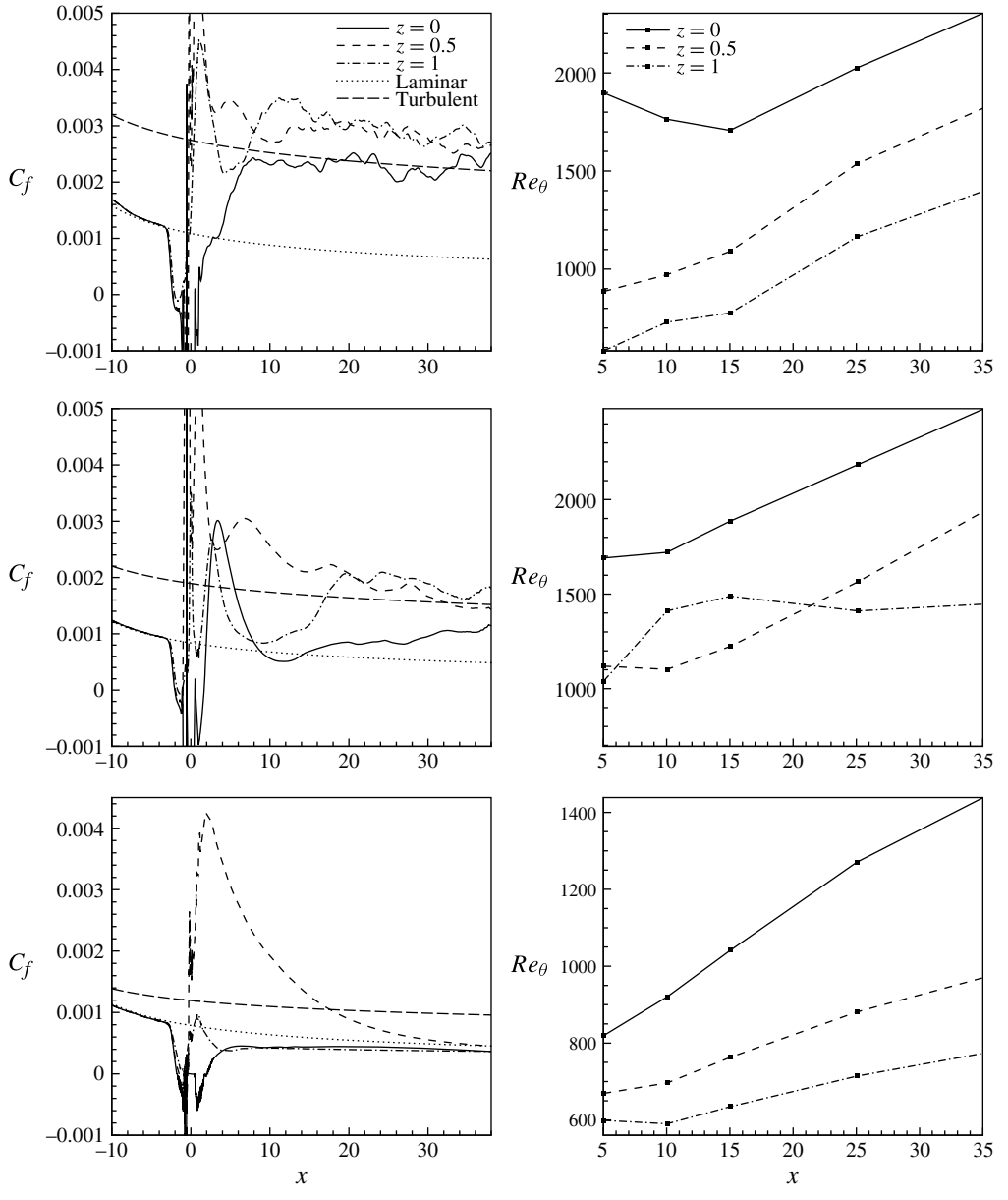

FIGURE 32. Mean skin-friction coefficient and Re_θ variation with x at $z = 0$, 0.5 and 1.0 for Mach 3.37, 5.26 and 8.23, respectively.

at $z = 0$ and 1, indicated by the rise in C_f. As for Mach 3.37, towards the outflow, the C_f curves appear to converge towards a single value indicating a turbulent flow. The variation of Re_θ is similar to the Mach 3.37 flow. For Mach 8.23, except at the location of the streamwise vortices, the C_f remains below the laminar value and approaches it with increasing downstream distance. At $z = 0.5$, the C_f increases sharply to about 4 times the laminar value and decreases with downstream distance

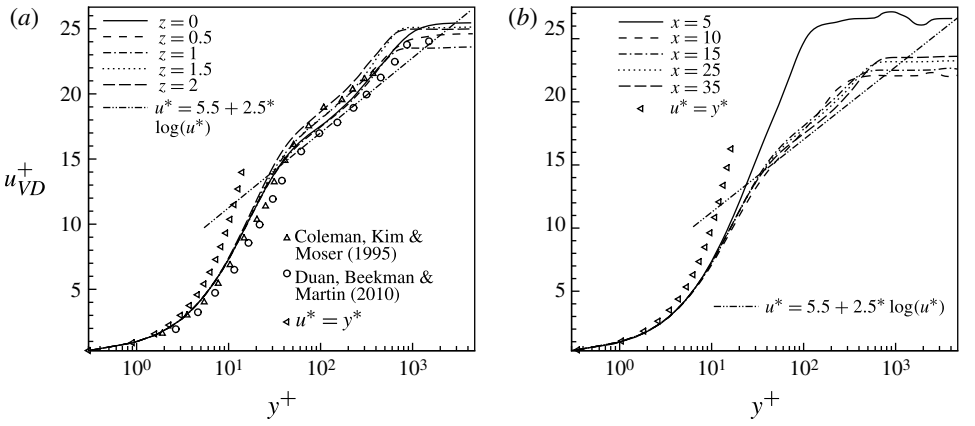

FIGURE 33. van Driest transformed velocity profiles at $x = 35$ (a) and $z = 1$ (b) for Mach 3.37.

Authors	M_∞	Re_θ	T_w/T_∞
Coleman, Kim & Moser (1995)	3	4880*	1
Duan, Beekman & Martin (2010)	4.97	1279.1	1
Spalart (1988)	—	1410	—

TABLE 5. Flow conditions for studies being compared in figures 33 and 34. (* Defined based on channel half-width and wall viscosity.)

approaching the laminar value. It is interesting that even for a flow that does not undergo transition, the effect of the roughness element is to cause a significant rise in C_f and C_h (figure 31) for a reasonable distance downstream.

Figure 33 shows profiles of the van Driest transformed velocity (u^+_{VD}) downstream of the roughness for Mach 3.37. The van Driest transformation is defined as

$$u^+_{VD} = \int \sqrt{\frac{\rho}{\rho_w}} \mathrm{d}u^+. \tag{6.2}$$

Also plotted are data from Coleman *et al.* (1995) and Duan *et al.* (2010) (table 5). Since the Mach 3.37 flow corresponds to a cold wall ($T_w/T_{aw} = 0.3$), the van Driest transformed velocity is compared with past studies with a similar wall condition. The shape of the curves resemble a fully developed turbulent boundary-layer profile. Note that the velocity profiles deviates from the linear law at around $y^+ = 2$ which appears to be typical of cold-wall turbulent boundary layers. Also, note that although the slope of the log-law matches well with the expected value, the intercept is slightly higher than the incompressible value. This again appears to be in line with expectations of a cold-wall flow as observed by Coleman *et al.* (1995). Note that the flow is still three-dimensional close to the outflow with small spanwise variations in the velocity profile. Also shown is the downstream evolution of the van Driest transformed profile at $z = 1$. Note that at $x = 5$, the profile resembles that of a laminar flow while with increasing distance downstream, the profile approaches that of a fully developed turbulent boundary layer.

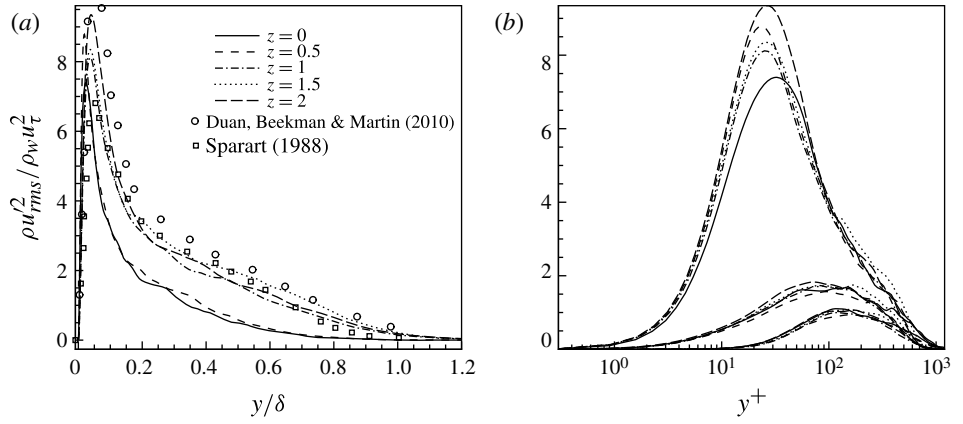

FIGURE 34. Reynolds stresses at $z = 0$, 0.5, 1, 1.5 and 2 and $x = 35$ for Mach 3.37.

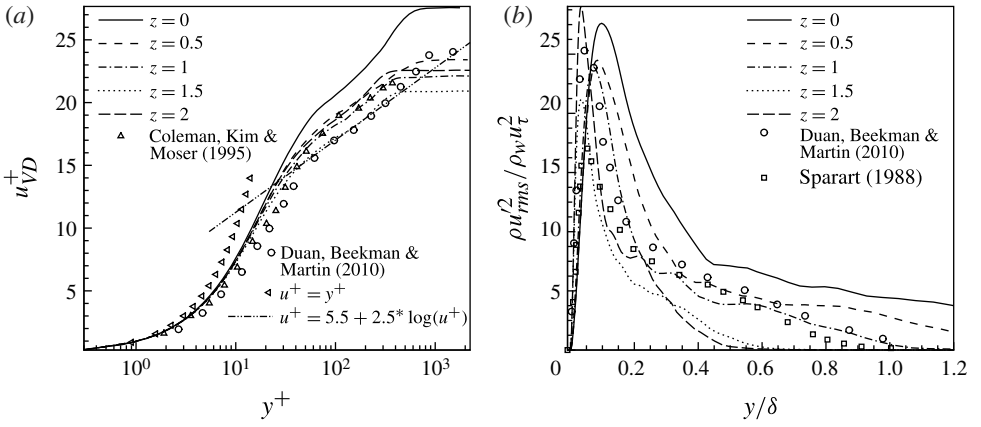

FIGURE 35. van Driest transformed velocity and Reynolds stress profiles at $z = 0$, 0.5, 1, 1.5 and 2 and $x = 35$ for Mach 5.26.

Figure 34 shows the variation of $\rho u'^2_{rms}/\rho_w u_\tau^2$ with y/δ and y^+ at $z = 0$, 0.5, 1, 1.5 and 2 and $35D$ from the roughness for Mach 3.37. δ was computed based on the location at which $u = 0.99u_\infty$. Also plotted are results from Duan *et al.* (2010) and Spalart (1988) for comparison. Good agreement is observed indicating that the flow is turbulent. Figure 35 shows the van Driest transformed velocity and Reynolds stress profiles at $x = 35$ for Mach 5.26. Note that the variation in z is greater for Mach 5.26 as compared to Mach 3.37.

6.8. *Local Reynolds number correlating with transition*

From the above discussions, the flow downstream of the hemispherical roughness element appears to undergo transition for Mach 3.37 and 5.26 and remains laminar for Mach 8.23. A combination of factors could be responsible for this behaviour at different flow conditions. Table 6 lists the free-stream Reynolds number for the three cases considered. It is known from stability theory that compressibility stabilizes the flow and our results are consistent with this with the lowest-Mach-number flow being

M_∞	Re_k	$Re_{k,wall}$	$E_{tr}^{0.5}$
3.37	9121	11364	614
5.26	14 190	4629	573
8.23	16 831	1104	415

TABLE 6. Values of Re_k, $Re_{k,wall} = u_\infty k/\nu_w$ and transient growth energy ($E_{tr}^{0.5}$) for the cases simulated.

most unstable and therefore undergoing transition to turbulence. It is also known in incompressible flows that a higher boundary layer thickness moves the transition point away from the roughness element due to the reduction in Re_k computed based on conditions at the roughness height and our results are consistent with this behaviour with the lowest boundary layer thickness case (Mach 3.37) transitioning closest to the bump. The free-stream Reynolds number based on roughness diameter (Re_k) is highest for Mach 8.23 which remains laminar. To account for the effect of boundary layer thickness and wall temperature, we compute a local Reynolds number based on free-stream velocity, wall kinematic viscosity and diameter of roughness ($Re_{k,wall} = u_\infty k/\nu_w$) and we see that this parameter is indicative of the trend observed for transition for the three cases. Mach 8.23 flow has the lowest $Re_{k,wall}$ while Mach 3.37 flow has the highest $Re_{k,wall}$.

We also quantify the potential for transient growth to examine whether it correlates with the behaviour of transition observed. From Reshotko & Tumin (2004), we know that transition occurs when E_{tr} reaches a specific value. Here E_{tr} is defined as follows:

$$(E_{tr})^{0.5} = (G^{0.5}/Re_\theta)Re_\theta(k/\theta)(T_e/T_w)^{0.5}. \tag{6.3}$$

Here $G^{0.5}/Re_\theta$ is obtained from figure 1 of Reshotko & Tumin (2004). The values of $E_{tr}^{0.5}$ from table 6 indicates that it correlates well with the observed trend of transition from the current DNS. Mach 3.37 flow undergoes transition closest to the roughness and has the highest value of E_{tr} and the 8.23 flow has the least E_{tr} and does not undergo transition.

7. Concluding remarks

The effects of an isolated hemispherical roughness element on a laminar high-speed boundary layer have been simulated for three Mach numbers wherein the highest-Mach-number flow remains laminar downstream and the lower-Mach-number flows undergo transition. Qualitative and quantitative comparison with experiments show good agreement. A qualitative mechanism for transition has been proposed. The three-dimensional separation of the boundary layer due to the presence of the roughness produces a shear layer and a system of vortices upstream and downstream of the bump. The unsteady counter-rotating streamwise vortices perturb the shear layer which break down further downstream to yield hairpin-shaped vortices. Hairpin-shaped structures are observed for the flows that transitioned. It was seen that for the Mach 8.23 flow, which did not transition, the counter-rotating vortices had a downwash between them which effectively reduced their strength with increasing downstream distance. The significant jump in skin-friction coefficient and wall heat transfer rates from the laminar value were used to confirm the transitional behaviour of the flow downstream of the bump. It was also seen that even for the flow that remained laminar downstream, the skin-friction coefficient and heat transfer rates could be significantly

higher immediately downstream of the bump for a reasonable distance downstream before it approaches the laminar value. The transfer of momentum and heat by the streamwise vortices is responsible for the significant rise in C_f and q_{wall} immediately downstream. Some spanwise variation in the flow close to the outflow was observed in the mean indicating the three-dimensional nature of the flow. The van Driest transformed velocity and Reynolds stresses indicated that the Mach 3.37 and Mach 5.26 flows behaved similar to a canonical turbulent boundary layer. Temporal wall-pressure spectra for Mach 3.37 flow showed that $St = 0.023$ was dominant upstream of the roughness, while downstream, the flow was highly unsteady and broadband with the nature of the curve far downstream resembling that of a canonical turbulent boundary layer. A local Reynolds number based on the wall properties appeared to correlate the tendency to transition when compared with the Reynolds number based on free-stream properties.

Acknowledgements

This work was partially supported by NASA under the hypersonics NRA program grant no. NNX08AB33A. Computer time for the simulations was provided by the Minnesota Supercomputing Institute (MSI) and Texas Advanced Computing Center through TeraGrid allocation. We thank Dr S. Muppidi for useful discussions, Dr A. Verma for help with mesh generation, and Dr Danehy and Mr Bathel for providing data from their experiments.

REFERENCES

ACARLAR, M. S. & SMITH, C. R. 1987 A study of hairpin vortices in a laminar boundary layer. Part 1. Hairpin vortices generated by a hemispherical protuberance. *J. Fluid Mech.* **175**, 1–41.

BAKER, C. J. 1979 The laminar horseshoe vortex. *J. Fluid Mech.* **95**, 347–367.

BARTKOWICZ, M. D., SUBBAREDDY, P. K. & CANDLER, G. V. 2010 Numerical simulations of roughness induced instability in the purdue mach 6 wind tunnel. *AIAA Paper* 2010-4723.

BATHEL, B. F., DANEHY, P. M., INMAN, J. A., WATKINS, A. N., JONES, S. B., LIPFORD, W. E., GOODMAN, K. Z., IVEY, C. B. & GOYNE, C. P. 2010 Hypersonic laminar boundary layer velocimetry with discrete roughness on a flat plate. *AIAA Paper* 2010-4998.

BERESH, S. J., HENFLING, J. F., SPILLERS, R. W. & PRUETT, B. O. M. 2011 Fluctuating wall pressures measured beneath a supersonic turbulent boundary layer. *Phys. Fluids* **23**, 075110.

CHANG, C. & CHOUDHARI, M. M. 2009 Hypersonic viscous flow over large roughness elements. *AIAA Paper* 2009-0173.

CHAI, X. & MAHESH, K. 2011 Simulations of high speed turbulent jets in crossflows. *AIAA Paper* 2011-650.

CHOI, H. & MOIN, P. 1990 On the space–time characteristics of wall-pressure fluctuations. *Phys. Fluids* A **2**, 1450.

CHOUDHARI, M. M., LI, F., WU, M., CHANG, C., EDWARDS, J., KEGERISE, M. & KING, R. 2010 Laminar-turbulent transition behind discrete roughness elements in a high-speed boundary layer. *AIAA Paper* 2010-1575.

COLEMAN, G. N., KIM, J. & MOSER, R. D. 1995 A numerical study of turbulent supersonic isothermal-wall channel flow. *J. Fluid Mech.* **305**, 159–183.

COLONIUS, T. 2009 Modelling artificial boundary conditions for compressible flow. *Annu. Rev. Fluid Mech.* **36**, 315–345.

DANEHY, P. M., BATHEL, B., IVEY, C., INMAN, J. A. & JONES, S. B. 2009 NO PLIF study of hypersonic transition over a discrete hemispherical roughness element. *AIAA Paper* 2009-394.

DANEHY, P. M., GARCIA, A. P., BORG, S., DYAKONOV, A. A., BERRY, S. A., INMAN, J. A. & ALDERFER, D. W. 2007 Fluorescence visualization of hypersonic flow past triangular and rectangular boundary-layer trips. *AIAA Paper* 2007-0536.

DONG, H. & ZHONG, X. 2002 High-order semi-implicit schemes for unsteady compressible flow simulations. *AIAA J.* **40** (5), 869–878.

DUAN, L., BEEKMAN, I. & MARTIN, M. P. 2010 Direct numerical simulation of hypersonic turbulent boundary layers. Part 2. Effect of wall temperature. *J. Fluid Mech.* **655**, 419–445.

ERGIN, F. G. & WHITE, E. B. 2006 Unsteady and transitional flows behind roughness elements. *AIAA J.* **44** (11), 2504–2514.

GROSKOPF, G., KLOKER, M. J. & MARXEN, O. 2008 Bi-global secondary stability theory for high-speed boundary layer flows. In *Proceedings of the Summer Program, Center for Turbulence Research*.

HUNT, J. C. R., WRAY, A. A. & MOIN, P. 1988 Eddies, stream, and convergence zones in turbulent flows. *Tech. Rep.* CTR-S88. Center for Turbulence Research.

KLEBANOFF, P. S., CLEVELAND, W. G. & TIDSTROM, K. D. 1992 On the evolution of a turbulent boundary layer induced by a three-dimensional roughness element. *J. Fluid Mech.* **237**, 101–187.

LEES, L. & LIN, C. C. 1946 Investigation of the stability of the laminar boundary layer in a compressible fluid. In *National Advisory Committee for Aeronautics*, Washington, DC.

MACK, L. M. 1984 Boundary-layer linear stability theory. In *AGARD Special Course on Stability and Transition of Laminar Flow*.

MALIK, M. R. 1990 Numerical methods for hypersonic boundary layer stability. *J. Comput. Phys.* **86** (2), 376–413.

MARXEN, O., IACCARINO, G. & SHAQFEH, E. S. G. 2010 Disturbance evolution in a Mach 4.8 boundary layer with two-dimensional roughness-induced separation and shock. *J. Fluid Mech.* **648**, 435–469.

MASON, P. J. & MORTON, B. R. 1987 Trailing vortices in the wakes of surface-mounted obstacles. *J. Fluid Mech.* **175**, 247–293.

MUPPIDI, S. & MAHESH, K. 2010 DNS of transition in supersonic boundary layers. *AIAA Paper* 2010-4440.

MUPPIDI, S. & MAHESH, K. 2011 DNS of unsteady shock boundary layer interaction. *AIAA Paper* 2011-724.

MUPPIDI, S. & MAHESH, K. 2012 Direct numerical simulations of roughness-induced transition in supersonic boundary layers. *J. Fluid Mech.* **693**, 28–56.

PARK, N. & MAHESH, K. 2007 Numerical and modelling issues in LES of compressible turbulent flows on unstructured grids. *AIAA Paper* 2007-722.

PIROZZOLI, S. & GRASSO, F. 2006 Direct numerical simulation of impinging shock waveturbulent boundary layer interaction at $M = 2.25$. *Phys. Fluids* **18**, 065113.

REDA, D. C. 2002 Review and synthesis of roughness-dominated transition correlations for reentry applications. *J. Spacecr. Rockets* **39** (2), 161–167.

REDFORD, J. A., SANDHAM, N. D. & ROBERTS, G. T. 2010 Compressibility effects on boundary-layer transition induced by an isolated roughness element. *AIAA J.* **48** (12), 2818–2830.

RESHOTKO, E. 2001 Transient growth: a factor in bypass transition. *Phys. Fluids* **13**, 1067.

RESHOTKO, E. 2007 Is Re_θ/M_e a meaningful transition criterion? *AIAA Paper* 2007-943.

RESHOTKO, E. & TUMIN, A. 2004 Role of transient growth in roughness-induced transition. *AIAA J.* **42** (4), 766–770.

SAKAMOTO, H. & HANIU, H. 1995 The formation mechanism and shedding frequency of vortices from a sphere in uniform shear flow. *J. Fluid Mech.* **287**, 151–171.

SARIC, W. S. 1994 Görtler vortices. *Annu. Rev. Fluid Mech.* **26**, 379–409.

SARIC, W. S., REED, H. L. & WHITE, E. B. 2003 Stability and transition of three-dimensional boundary layers. *Annu. Rev. Fluid Mech.* **35**, 413–440.

SCHNEIDER, S. P. 2008 Effects of roughness on hypersonic boundary-layer transition. *J. Spacecr. Rockets* **45** (2), 193–209.

SIMPSON, R. L. 2001 Junction flows. *Annu. Rev. Fluid Mech.* **33**, 415–443.

SPALART, P. R. 1988 Direct simulation of turbulent boundary layer up to $R_\theta = 1410$. *J. Fluid Mech.* **187**, 61–98.

TANI, I., KOMODA, H., KOMATSU, Y. & IUCHI, M. 1962 Boundary-layer transition by isolated roughness. In *Report* No. 375. Aeronautical Research Institute, University of Tokyo.

TUMIN, A. & RESHOTKO, E. 2005 Receptivity of a boundary-layer flow to a three-dimensional hump at finite Reynolds numbers. *Phys. Fluids* **17**, 094101.

YEE, H. C., SANDHAM, N. D. & DJOMEHRI, M. J. 1999 Low-dissipative high-order shock-capturing methods using characteristic-based filters. *J. Comput. Phys.* **150** (1), 199–238.

ZHONG, X. 1998 High-order finite-difference schemes for numerical simulation of hypersonic boundary-layer transition. *J. Comput. Phys.* **144** (2), 662–709.

ZHONG, X. & WANG, X. 2012 Direct numerical simulation on the receptivity, instability, and transition of hypersonic boundary layers. *Annu. Rev. Fluid Mech.* **44**, 527–561.